

Local Time Asymmetries in the Venus Thermosphere

M. J. ALEXANDER,¹ A. I. F. STEWART, AND S. C. SOLOMON

Laboratory for Atmospheric and Space Physics, University of Colorado, Boulder

S. W. BOUGHER

Lunar and Planetary Laboratory, University of Arizona, Tucson

The bright emission at 130 nm from atomic oxygen in the Venus thermosphere, as measured by the Pioneer Venus Orbiter Ultraviolet Spectrometer (PVOUVS), can serve as a diagnostic of Venus thermospheric structure. Images from the PVOUVS at this wavelength reveal unusual large-scale patterns in the emission which can be interpreted as variations in the O/CO₂ ratio in the middle thermosphere. Through analysis of these images, a high-contrast asymmetry in local time has been revealed which has not previously been observed or predicted by any existing models. The asymmetry can be interpreted as typically a factor of 2 increase in oxygen densities at the nighttime terminator over corresponding day times, and this basic pattern has been present in every image examined, spanning the period 1980–1990. The pattern in local time is not present at equatorial latitudes less than ~30° but appears in both the northern and southern hemispheres poleward of 30°. This local time asymmetry in O can be understood in the context of the subsolar-to-antisolar flow pattern which dominates the thermospheric circulation: gravity waves, originating in the middle atmosphere of Venus where a westward zonal flow pattern dominates, will preferentially enhance eddy mixing in the morning hours if these waves propagate into the thermosphere. Enhanced eddy mixing tends to lower thermospheric O. This same mechanism can also explain zonal asymmetries known to be present in the thermospheric subsolar-to-antisolar wind pattern (Alexander, 1992).

1. INTRODUCTION

The Pioneer Venus Orbiter Ultraviolet Spectrometer (PVOUVS) has returned data on the upper atmosphere of Venus from December 1978 until October 1992. Beginning in 1980, the instrument primarily operated in the fixed-wavelength mode [Stewart, 1980], where an image of the planet at a particular wavelength could be created at each of two viewing periods during the orbit. Images at 130 nm of the dayside show the bright emission from the resonance transition in atomic oxygen. O is one of the main constituents in the Venus thermosphere and becomes the dominant constituent 15–20 km above the homopause, where molecular diffusive processes are important. CO₂, which dominates the lower atmosphere, absorbs the O I 130-nm emission below ~125 km. Sources for O in the thermosphere are photodissociation of CO₂ and dissociative recombination in the ionosphere. Recombination of the dissociation products, O and CO, does not efficiently occur until they are transported, by a combination of the large-scale subsolar-to-antisolar circulation and small-scale eddy mixing, to altitudes below ~100 km. Our modeling of the O I emission at 130 nm shows the brightness is primarily controlled by the O/CO₂ ratio in the middle thermosphere. This ratio is, in turn, sensitive to turbulent mixing processes and large-scale wave activity there. Thus we can use the 130-nm images from the PVOUVS to study the structure and dynamics of the Venus thermosphere. The images provide a picture of atomic oxygen in the thermosphere over a wide range of latitudes

and local times at frequent intervals throughout the last 12 years. The analysis in this paper spans the interval 1980–1990.

The structure of the Venus thermosphere, to first order, is fairly well determined. The Pioneer Venus mission has been responsible for considerable advances in our understanding of thermospheric composition and dynamics. Measurements of composition by the orbiter neutral mass spectrometer (PVONMS [Neumann et al., 1980]) have been incorporated into a global empirical model of neutral densities and temperatures called the VTS3 [Hedin et al., 1983]. This model incorporates a 1.63 density correction factor to the neutral density measurements based on measurements of total density by the Pioneer Venus orbiter atmospheric drag experiment (PVOAD [Keating et al., 1980]). The VTS3 is widely available in the form of a Fortran subroutine. VIRA [Keating et al., 1985] is another empirical model developed in an attempt to synthesize all of the available information from Pioneer Venus and Venera 11 and 12. This model applies slightly different normalization factors to the PVONMS densities: 1.83 for CO₂, and 1.58 for O, CO, N₂, and N. The largest differences between VIRA and VTS3 are the vertical profiles of O and CO in the lower thermosphere (below 125 km). VIRA is based on one-dimensional photochemical results [Massie et al., 1983] at these altitudes and gives dayside O densities an order of magnitude larger than VTS3 at 110 km. The emission at 130 nm (which is the focus of this paper) is, however, insensitive to these differences in the lower thermosphere.

These observations and models, as well as measurements by the PVOUVS [Stewart et al., 1979, 1980] have provided crucial constraints for the development of the three-dimensional (3-D) Venus thermospheric general circulation model (VTGCM [Bougher et al., 1990]). (Note, however, that thermospheric densities and temperatures are still un-

¹Now at the Department of Atmospheric Sciences, University of Washington, Seattle.

Copyright 1993 by the American Geophysical Union.

Paper number 93JE00538.
0148-0227/93/93JE-00538\$05.00

certain over much of the globe, since measurements by the PVONMS and PVOAD were restricted to a narrow latitude band near 15°N and only at solar activity levels near maximum.) The existence of the basic subsolar-to-antisolar (SS-AS) flow pattern was established on theoretical grounds 20 years ago by *Dickinson* [1971]. This picture of a purely symmetric flow pattern has been revised by observations of the hydrogen and helium nightside bulges [*Brinton et al.*, 1980; *Neumann et al.*, 1980] and of the NO nightglow [*Stewart et al.*, 1980; *Bougher et al.*, 1990], which suggest that the convergence on the nightside is offset from the antisolar point to about 0200–0300 local time. These observations have lead to the theory of a zonal superrotation component of the thermospheric winds.

The origin of the thermospheric superrotation has long been considered to be unknown [*Fox and Bougher*, 1991]. A recently proposed mechanism by *Alexander* [1992] produces a superrotation forcing which resembles the empirical formulation in the VTGCM [*Bougher et al.*, 1988]. Thermospheric modelers have largely circumvented the question of origin and focused instead on characterizing the properties of the superrotation [*Mayr et al.*, 1985; *Bougher et al.*, 1988, 1990; *Mengel et al.*, 1989]. Predictions of the speed of the SS-AS winds have been steadily decreasing since the early Dickinson model via the inclusion of Rayleigh friction to represent wave drag [*Bougher et al.*, 1988, 1990; *Mengel et al.*, 1989]. These modifications were introduced to reproduce the observed cold nightside temperatures and day/night density contrasts. Current estimates suggest the SS-AS winds reach 100–230 m s⁻¹ across the terminators, and the zonal superrotation speed is 50–75 m s⁻¹ at the equator.

We can now add the set of PVOUVS images of the O I 130-nm dayglow as a new constraint for the VTGCM. The analysis of these images reveals stable patterns in thermospheric atomic oxygen, which are locked in local solar time and latitude, and have persisted since 1980, when the first 130-nm images were acquired. The pattern in O appears as an asymmetry between morning and afternoon hours with O densities ~80% higher at 1600 than at 0800 local time (at 60°N latitude). Our hypothesis is that the stable subsolar-to-antisolar flow pattern coupled to a steady supply of gravity waves from the middle atmosphere can provide the asymmetric eddy diffusion necessary to explain the asymmetry in O on the dayside. If this mechanism is active, a corollary effect on the thermospheric winds would also be present: Differential wave drag between morning and afternoon local times could produce an asymmetry in the winds sufficient to explain the superrotation and the offset of the antisolar convergence to the early morning hours on the nightside. This wave drag effect has been developed by *Alexander* [1992].

Our approach is to first compare the PVOUVS images to model predictions which incorporate current understanding of the global structure of the thermosphere, the mechanisms which excite the 130-nm transition in O, and the radiative transport of the 130-nm triplet in the thermosphere. The model is similar to that used by *Stewart et al.* [1992] in the analysis of the 130-nm emission from Mars as measured by the Mariner 9 ultraviolet spectrometer. The comparison of the PVOUVS data to the model reveals patterns in the O/CO₂ ratio which deviate from the expected solar zenith angle dependent trend like that observed by the PVONMS and predicted by the VTGCM. Because of statistical varia-

tions in the data associated with low count rates, we are limited to studying large- to planetary-scale features in the images: those with horizontal scales $\sim O(1000 \text{ km})$. The observed patterns in the O/CO₂ ratio can be grouped into two broad categories: (1) features locked in local solar time and latitude which are present in nearly every image at 130-nm, and (2) more transient features which change in form and/or location from image-to-image. In this paper we focus on the solar-locked patterns by examining long-term averages of the data/model ratio mapped in latitude versus local time, and compare the results to existing global thermospheric models [*Bougher et al.*, 1988; *Hedin et al.*, 1983].

To interpret these results, we relate the effects of gravity wave saturation to thermospheric structure via the *Lindzen* [1981] parameterization for eddy diffusion as modified by *Holton* [1982]. The same middle atmosphere sources for gravity waves saturating in the thermosphere as proposed by *Alexander* [1992] to explain the origin of the thermospheric superrotation, are used here to explain the O asymmetries observed in the PVOUVS 130-nm images.

In section 2 we discuss the PVOUVS instrument and the 130-nm image data set. Section 3 describes our model of the 130-nm emission from atomic oxygen and the relationship of O density to brightness at this wavelength. The results of the 130-nm image data-to-model comparison are presented in section 4, and compared to existing thermospheric models. In section 5 we discuss the hypothesis of gravity wave saturation in the thermosphere as an explanation for the morning/afternoon asymmetries in O densities, and section 6 is a summary of the results and discussion.

2. PVOUVS 130-NM IMAGES

2.1. PVO Orbit and UVS Imaging

The Pioneer Venus Orbiter (PVO) is in an elliptical orbit approximately perpendicular to the plane of the ecliptic ($i = 105^\circ$), with an orbital period of 24 hours. The UVS is mounted at a 60° angle from the spacecraft spin axis which is roughly oriented in the direction of the south ecliptic pole. As the spacecraft spins at a rate of ~ 13 s per revolution, the UVS line of sight moves through 360° of ecliptic longitude. The orbit geometry and imaging capabilities are described by *Stewart* [1980]. There are two periods during each 24-hour orbit when the instrument line of sight intersects the planet.

2.1.1. PVOUVS inbound images. The first imaging period begins after the spacecraft has passed through apoapsis and is approaching Venus. The line of sight first acquires the southern limb, then builds up an image as a series of west-east scans marching toward the North Pole. While the image is being created, the spacecraft is moving closer to the planet, so that Venus subtends a larger angle at the north end of the image than at the south. The finite area of the instrument slit (6.0 mm \times 0.625 mm, or 1.4° \times 0.14°) projected onto the surface also means the spatial resolution of these images improves from south to north. These “inbound images” display $\sim 2\pi$ of Venus in every image, so they can be used to examine horizontal structure in thermospheric emissions on a daily basis. The early inbound images were acquired over a period of 1.5 hours (centered at 75 min before periapsis), and this increased to 3 hours (centered at 5 hours before periapsis) in the more recent inbound images. The change is due to a precession of the line of apsides of the

orbit. The instrument slit is oriented with the long axis approximately north to south, so the southern end of these images suffers greatly from “slit smear,” when the photon count rate varies widely over the aperture. Measurements of the southern edge of these images average the bright limb with empty space, making these observations difficult to model. The model described in section 3 takes this slit smear into account; however, minor errors in the reported pointing geometry preclude accurate modeling there. Thus the inbound images provide a clear view of ~12 hours of local time and of latitudes from ~30°S to the North Pole.

2.1.2. PVOUVS periapsis images. The second imaging period is centered about periapsis starting at the north and ending at the south limb. These images are acquired over a 30-min period centered near periapsis. Since the spacecraft is much closer to the planet, the spatial resolution is much higher than in the inbound images, and problems with slit smear are minimized. However, each scan from horizon to horizon covers only a limited range of local times. During the first 600 orbits, the spacecraft dipped into the thermosphere during periapsis, allowing in situ measurements of density with the mass spectrometers and drag experiment. Thereafter periapsis was allowed to rise, so that the brightness measurements in both the inbound and periapsis UV images represent total column emission rates as measured by an observer outside the atmosphere. These images from outside of the atmosphere can be accurately represented by our model, which is described section 3.

2.2. Image Rectification and Mapping

The inbound image data are rectified for visual image analysis. An example from orbit 1200 is shown as a kilo-Rayleigh contour map in Figure 1a. The simple procedure we use projects the minimum ray height vector onto the plane perpendicular to the spacecraft/Venus position vector. (The minimum ray height vector is drawn from the center of Venus, perpendicular to the line-of-sight vector.) This rectification preserves the minimum distance between the line of sight and the center of Venus, and retains the azimuth angle between the minimum ray height projection and the spin axis projection onto the image plane. (The spacecraft spin axis has been maintained in close alignment with the north-south ecliptic axis throughout the mission.) The brightness values and associated geometric parameters (view angle, solar zenith angle, solar latitude, and solar longitude) are binned into 128×128 image arrays for convenience of storage. For the inbound data, the result is an image which closely resembles a photograph of a globe; however, the motion of the spacecraft along its orbit while the image data are assembled means longitude meridians and latitude contours are slightly distorted. (The distortion is so slight that it is hard to detect visually. See Figure 1b.) The orbital inclination ($i = 105^\circ$) means a slightly different range of longitudes is viewed in the north than in the south, and the changing spacecraft/Venus vector means the image plane tilts backward as the spacecraft moves northward, acquiring data. The simplicity and near accuracy of this procedure make it a useful tool for examining the PVOUVS data visually. The images provide a global view of the thermospheric UV emission patterns.

Another useful way to examine the data (either inbound or periapsis) is by mapping it into an array of solar longitude

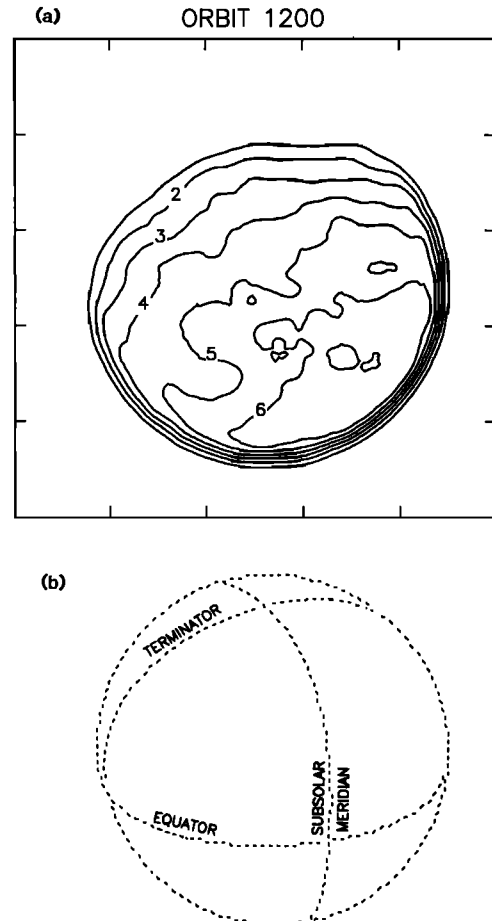


Fig. 1. (a) Contour plot of the rectified image for orbit 1200 showing 130-nm column brightness in kilo-Rayleighs. The image has been smoothed for clarity of presentation. (b) Associated geometry for the image in Figure 1a.

and latitude. The observations must first be normalized to a model which accurately describes limb brightening. This prevents geometrical effects on the measured brightness from contaminating the resulting patterns in the map. The model used for this purpose will be described later, in section 3. The mapping procedure finds the predicted model intensity (given the view angle and solar zenith angle associated with each observation), ratios data to model value, and stores the results in a 30×30 array in local time and latitude. The number of measurements stored in each bin is also cataloged for statistical purposes and for subsequent averaging procedures. Local time ranges from 6 to 18 hours, and latitude from -55° to $+80^\circ$. This procedure also removes the subsolar-to-terminator darkening effect and allows examination of the anomalous patterns. Observations with a solar zenith angle greater than 80° are not retained because of the difficulties associated with modeling the terminator region. (None of the global models claim to accurately portray this region.) Observations with viewing angles beyond 85° are also discarded (see section 2.3). This same mapping procedure can be performed on both raw and rectified images. The maps will be used to observe solar-locked features in the data (section 4.2) by first performing a long-term average on a collection of them. The individual orbit maps must first be normalized for day-to-day solar

activity variations before the averaging is performed (see section 3.4.3).

2.3. Image Geometry

The geometry for the rectified image from orbit 1200 (Figure 1a) is shown in Figure 1b. (The unsmooth appearance of the geometry contours simply reflects the finite bin size in the array.) The equator and subsolar meridian intersect at approximately the subsolar point, since Venus' spin axis is tilted only 3° from the north-south ecliptic axis. Contours of constant viewing angle would appear as concentric circles about the center of the image. The planet appears tilted toward the viewer approximately 30°, so that latitudes south of 60° cannot be observed. The PVO orbit is fixed in inertial space, so the local time of periapsis drifts through a 24-hour cycle every 225 days (= 1 Venus year). This results in a slowly varying phase angle of the images of 1.6° per orbit.

The accuracy of the reported geometry associated with the UV measurements is limited by uncertainties in the spacecraft spin axis and spin rate. These errors result in offsets and distortions in the comparison between the PVOUVS rectified images and the geometric disc. Over most of the planet, these errors are small enough to be ignored, but at the limb, accuracy becomes critical. The images in this analysis have all been corrected to match the reported geometry by manual centering. Residual distortions are then minimized by neglecting observations within 5° of the limb. This is not a serious limitation: over 99% of the image area is retained, and the rejected limb observations from outside of the atmosphere are already seriously degraded by slit smear.

2.4. Instrument Sensitivity

The images of Venus at 130 nm are acquired while the OUVS is operating in "fixed-wavelength mode." *Stewart* [1980] describes the instrument design and capabilities in detail. The PVOUVS is a grating spectrometer with two detectors sensitive to wavelengths 110 to 180 nm with the *G* channel and 160 to 330 nm with the *F* channel detector. The grating can be rotated in 0.44-nm steps continuously to produce spectra, or can be commanded to move to a particular grating position (GP) and hold to create images at a selected wavelength. When the grating is set to detect the 130-nm emission, the 1.3-nm spectral resolution of the instrument spreads the response to the O I triplet out over six GP's between 129- and 132-nm wavelength. On orbits 1611 and 1653 the instrument grating was stepped across this range of wavelengths to measure the response to the 130-nm triplet as a function of GP. These measurements provide a relationship between the intensity at a given grating position and the total intensity in the 130-nm triplet, which is needed to interpret the image data.

The peak response for the 130-nm O I triplet was measured at GP 59, so this setting was selected for most of the 130-nm image data. Near orbit 3250, the prime grating control unit (GCU) developed an instability at GP 59, so that the GCU repeatedly failed to hold the grating at this position. The 130-nm imaging was then done at GP 60 until orbit 3960, when GP 60 also became unstable. Thereafter, GP 61 was routinely used to image Venus in the 130-nm triplet. There was a backup GCU, but it too has similar instabilities. For

orbits 3279 through 3307, 130-nm imaging was performed using GP 62 on the backup GCU. The response curve for the backup GCU was not determined until an instability at the peak GP had already developed. This precluded normalization of the integrated response to the calibration value, leaving the GP versus sensitivity relationship uncertain. We have interpolated across the unstable GP on the backup GCU and then normalized the total area under the response curve to match that of the prime GCU minispectrum. Table 1 lists the instrument sensitivity versus GP for both the prime and backup GCU's derived from this procedure and normalized to match the calibration value of 0.95 counts/kR/4 ms at GP 59 of the prime GCU.

2.5. Instrument Calibration and Uncertainties

The PVOUVS has been through two in-flight stellar calibrations, in July 1978 and April 1984. The *G* channel response was shown to be remarkably stable over this period. Values for sensitivity have been determined using the rocket measurements of *Brune et al.* [1979] as an absolute standard. Thus the absolute uncertainty in the standard approximately determines the absolute uncertainty in the *G* channel sensitivity and has been estimated at ±20%.

The relative uncertainty between any two measurements follows Poisson statistics, so the fractional standard deviation is $N^{-1/2}$, where N is the number of counts measured by the detector. The image shown in Figure 1 has been smoothed to suppress this statistical noise. Images acquired at GP 59 have a standard deviation of $\sigma \sim 10\text{--}15\%$ across most of the sunlit hemisphere, while at GP 61, $\sigma \sim 15\text{--}25\%$. Thus several pixels must be averaged together to reduce the statistical noise. A 3×3 smoothing reduces the standard deviation to 3–5% at GP = 59, and to 5–8% at GP = 61. After smoothing, we cannot focus on small-scale variations ($\sim 10^2$ km) in these images but are restricted to studying variations with scales $\geq 10^3$ km. For reference, the rectified images have a resolution of ~ 100 km, and 10° latitude ≈ 1000 km on Venus.

2.6. The 130-nm Observations

Regular imaging sequences with the PVOUVS instrument operating in the fixed-wavelength mode began in 1980. Thereafter, observations generally followed a weekly cycle,

TABLE 1. Sensitivity Versus Grating Position

Grating Control	Grating Position	λ , nm	Sensitivity*
Prime	57	129.11	0.09
Prime	58	129.60	0.49
Prime	59	130.04	0.95
Prime	60	130.58	0.78
Prime	61	131.06	0.43
Prime	62	131.55	0.20
Backup	59	129.00	0.04
Backup	60	129.49	0.21
Backup	61	129.97	0.50
Backup	62	130.46	0.71
Backup	63	130.95	0.76
Backup	64	131.44	0.50
Backup	65	131.92	0.32

*In units of counts/kR/4 ms.

including one 130-nm image per week. An example series of such images from the spring of 1982 is shown in Plate 1. The changing phase angle of the observations is apparent as the observations progress from the morning to the afternoon terminator. Note the interesting brightness features which appear and disappear from week to week, and the irregularities in brightness along the terminators.

Table 2 lists the orbit numbers and dates of the observations included in this analysis. In total, 56 inbound images and 42 periapsis images have been examined. These tend to be grouped in series like the one shown in Plate 1. The observations span 10 years, a period which covers nearly an entire solar activity cycle, but with sizable gaps. About 2.5 months of Pioneer Venus observing time was devoted to comet Halley in 1986 which partly explains the lack of a coherent set of planetary observations in this time period. In recent years (1990 to present) interruptions in Pioneer Venus tracking time due especially to the Galileo and Magellan missions have made it difficult to acquire the kinds of complete global images required in this analysis.

Also noted in Table 2 is the type of data, either inbound or periapsis. These two sets were handled separately because of the differences in their attributes and limitations. The inbound images are exploited for their more global view of Venus on every orbit, while the periapsis data provide the high spatial resolution which the inbound images lack, especially at southern latitudes.

3. MODELING THE 130-NM IMAGES

3.1. Problem Overview

The PVOUVS 130-nm images such as those shown in Plate 1 contain information about the Venus thermosphere. The 130-nm emission comes from thermospheric atomic oxygen, which is one of the main atmospheric constituents at these altitudes, so the global characteristics of the brightness should be able to tell us something about the general structure of the thermosphere. In addition, the unusual large-scale brightness features, which appear and disappear from week to week, hint that large-scale dynamics are somehow perturbing the thermosphere. For this 130-nm radiative transfer problem, the thermosphere can be thought of as a simple two-component atmosphere with O as the scatterer and CO₂ as the absorber. The standard vertical profiles which will be used in the models to be described in this section are shown in Figure 2.

In 1980, when these images were first acquired, the large optical depths at this wavelength made the interpretation of these measurements a formidable radiative transfer problem. The radiative transfer techniques available at that time (which included assumptions of an isothermal atmosphere and of complete frequency redistribution) could not accurately represent the observations [Strickland, 1979; Lee and Meier, 1980]. In addition, models of global thermospheric structure [Dickinson, 1971; Dickinson and Ridley, 1975, 1977; Mayr et al., 1978] had not yet incorporated the wealth of knowledge gathered during the early years of the Pioneer Venus mission.

Since that time, radiative transfer analysis of the oxygen resonance triplet has evolved considerably [Meier and Lee, 1982; Gladstone, 1988; Meier, 1991], accounting for important effects of atmospheric temperature gradients and partial

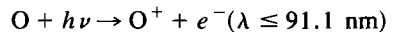
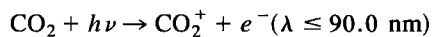
frequency redistribution in the scattering process. A number of global thermospheric models are now available. The VTS3 [Hedin et al., 1983] and VIRA [Keating et al., 1985] empirical models describe thermospheric neutral densities and temperatures based on in situ measurements of the Pioneer Venus orbiter. It is important to note that the densities in these empirical models are based on actual measurements only in a narrow band of latitudes, a few degrees either side of 16° north. Studies of the thermospheric circulation have evolved to fully three-dimensional self-consistent determinations of winds, densities, and temperatures [Bougher et al., 1986, 1988, 1990; Mayr et al., 1980, 1985; Mengel et al., 1989].

Our analysis of the 130-nm images uses what is already known about the Venus thermosphere from the VTS3 and VTGCM, coupled to the radiative transfer techniques of Meier and Lee [1982] to create synthetic images for comparison to the data. The synthetic images represent the smoothed global-scale trends seen in the images, but do not attempt to reproduce the anomalous features obvious in the data. Comparing these models to the data gives us a unique global view of the distribution of atomic oxygen on the dayside of Venus, spanning a time period comparable to the 11-year solar activity cycle.

3.2. Excitation Mechanisms

On the dayside in the Venus thermosphere, O is excited to the ${}^3S^0$ state by two primary mechanisms: (1) excitation by impact with energetic photoelectrons and (2) resonance scattering of solar 130-nm photons. The first will be referred to as "photoelectron," and the second as "solar." These two sources of excitation are of comparable importance to the 130-nm emission from Venus (depending upon the geometry of the particular observation), though the photoelectron source generally contributes the larger fraction to the emergent intensity. Other possible sources from CO and CO₂, as listed in Fox and Bougher [1991], are negligible compared with the excitation rates computed in the present analysis.

3.2.1. Photoelectron impact excitation. The most important source for the 130-nm emission from Venus is excitation of O by impact with energetic photoelectrons. Solar photons with energies greater than 13.6 eV ($\lambda \leq 91$ nm) can produce energetic photoelectrons as they ionize the neutral atoms and molecules in the upper atmosphere. The most important photoionization reactions on Venus are



Other less important sources for photoelectrons are photo-dissociative ionization of CO₂, and photoionization of CO, N₂, and NO. The newly created electron carries away most of the excess photon energy as kinetic energy. With a spectrum of incoming solar photons, and a suite of photoionization processes, the result is a spectrum of photoelectrons which will vary with altitude. The electrons with kinetic energies greater than 9.5 eV can excite the O atom to $O({}^3S^0)$, which will subsequently emit a 130-nm photon as O decays back to the ground state, $2p\ {}^3P$. More energetic electrons can excite O to higher energy states, some of which will relax to the ${}^3S^0$ state. This contribution to ${}^3S^0$ state excitation is called the cascade contribution. (See

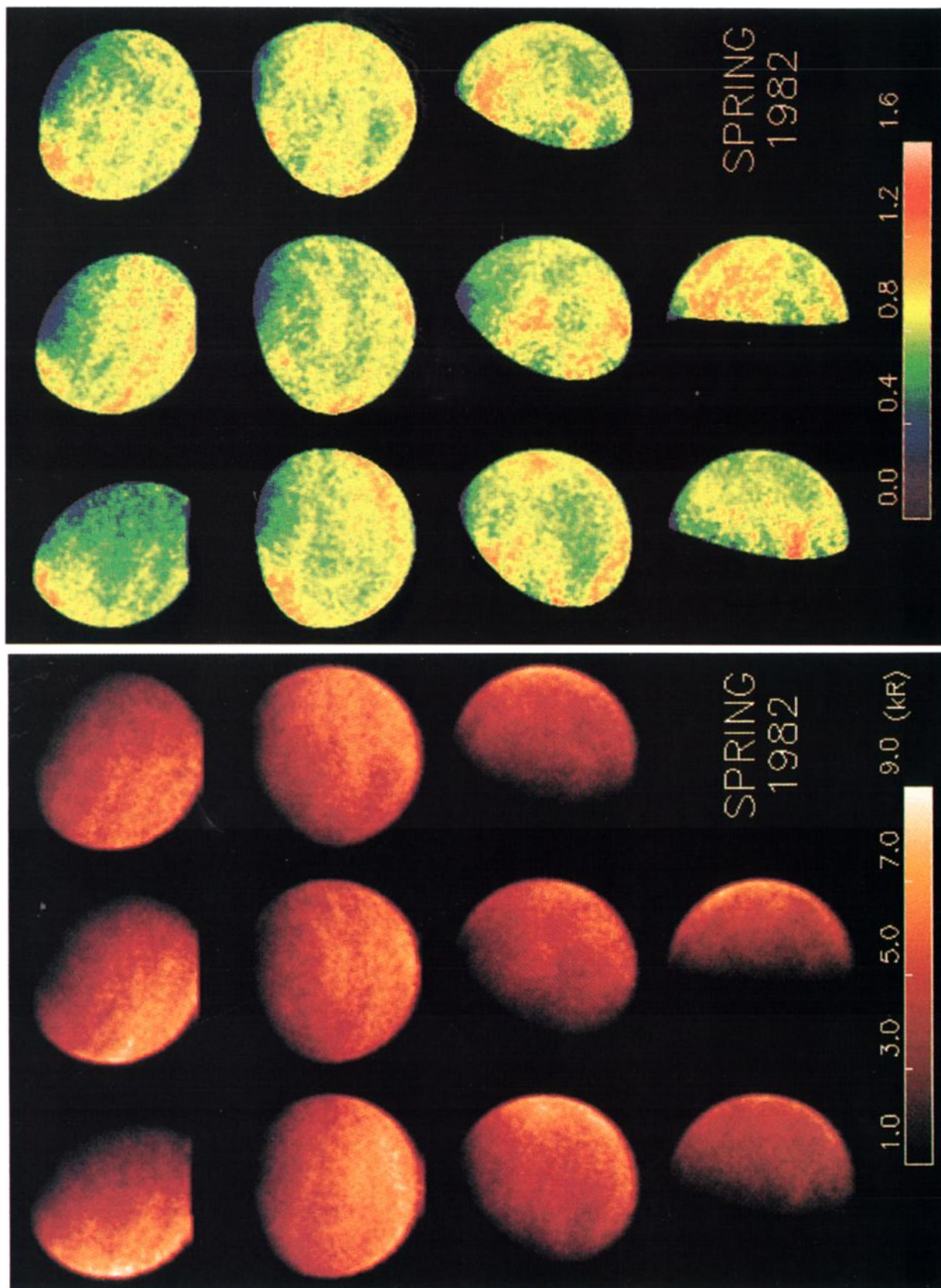


Plate 1. Rectified images from February–May 1982. Images (from left to right and top to bottom) are from orbits 1158, 1165, 1172, 1186, 1193, 1200, 1214, 1221, 1228, 1235, and 1242.

Plate 2. Ratio image (data/model) for the same image series as shown in Plate 1.

TABLE 2. PVOUVS 130-nm Observations

Orbit No.	Date as YYDOY	Type of Data Stored	Local Time at 30°N*	VF _{10.7} Index
477	80087	Inbound image	8.0	219.00
484	80094	Inbound image	8.7	176.34
491	80101	Inbound image	9.5	197.06
498	80108	Inbound image	10.3	213.37
505	80115	Inbound image	11.0	193.74
512	80122	Inbound image	11.7	195.31
519	80129	Inbound image	12.6	219.23
523	80133	Inbound image	13.0	198.40
533	80143	Inbound image	14.1	228.97
540	80150	Inbound image	14.8	206.78
547	80157	Inbound image	15.6	197.62
711	80321	Inbound image	9.0	225.48
712	80322	Inbound image	9.1	224.65
713	80323	Inbound image	9.2	218.68
715	80325	Inbound image	9.4	205.46
716	80326	Inbound image	9.5	193.45
717	80327	Inbound image	9.6	189.58
718	80328	Inbound image	9.7	190.44
1158	82037	Inbound image	8.7	222.57
1165	82044	Inbound image	9.5	183.46
1172	82051	Inbound image	10.2	168.35
1186	82065	Inbound image	11.7	205.34
1193	82072	Inbound image	12.6	183.05
1200	82079	Inbound image	13.3	179.91
1214	82093	Inbound image	14.8	182.80
1221	82100	Inbound image	15.5	159.09
1228	82107	Inbound image	16.2	161.88
1235	82114	Inbound image	17.0	150.54
1242	82121	Inbound image	17.7	161.76
1298	82177	Periapsis image	10.4	177.56
1305	82184	Periapsis image	11.2	152.86
1312	82191	Periapsis image	11.8	133.92
1319	82198	Periapsis image	12.7	158.42
1333	82212	Periapsis image	14.2	164.10
1340	82219	Periapsis image	15.0	139.09
1347	82226	Periapsis image	15.7	172.84
1706	83220	Periapsis map	6.1	123.12
1707	83221	Periapsis map	6.2	124.38
1709	83223	Periapsis map	6.4	134.67
1710	83224	Periapsis map	6.5	137.31
1711	83225	Periapsis map	6.6	138.63
1716	83230	Periapsis map	7.1	130.77
1717	83231	Periapsis map	7.2	123.12
1721	83235	Periapsis map	7.7	121.55
1723	83237	Periapsis map	7.9	115.67
1724	83238	Periapsis map	8.0	113.20
1728	83242	Periapsis map	8.4	114.46
1731	83245	Periapsis map	8.7	110.82
1732	83246	Periapsis map	8.8	108.43
1739	83253	Periapsis map	9.6	124.44
1746	83260	Periapsis map	10.3	110.82
1753	83267	Periapsis map	11.0	108.43
1760	83274	Periapsis map	11.7	106.06
1774	83288	Periapsis map	13.2	120.61
1788	83302	Periapsis map	14.8	99.08
1795	83309	Periapsis map	15.5	110.82
1802	83316	Periapsis map	16.3	113.23
1809	83323	Periapsis map	17.0	108.43
1816	83330	Periapsis map	17.8	92.30
2103	84252	Inbound image	13.6	77.17
2105	84252	Inbound image	13.9	73.02
2264	85047	Inbound image	6.7	81.39
2271	85054	Inbound image	7.5	79.27
2306	85089	Inbound image	11.3	85.69
2327	85110	Inbound image	13.6	87.87
2341	85124	Inbound image	15.0	77.17
3279	87332	Periapsis map	6.0	80.33
3293	87346	Periapsis map	7.4	87.87
3307	87360	Periapsis map	8.9	88.97
3328	88016	Periapsis map	11.1	88.97
3342	88030	Periapsis map	12.7	108.43
3349	88037	Periapsis map	13.4	113.24

TABLE 2. (continued)

Orbit No.	Date as YYDOY	Type of Data Stored	Local Time at 30°N*	VF _{10.7} Index
3356	88044	Periapsis map	14.2	107.24
3363	88051	Periapsis map	14.9	101.39
3377	88065	Periapsis map	16.5	107.24
3384	88072	Periapsis map	17.2	113.24
3391	88079	Periapsis map	18.0	107.24
3603	88291	Inbound image	5.7	137.31
3615	88303	Inbound image	7.0	126.92
3617	88305	Inbound image	7.2	126.92
3624	88312	Inbound image	7.9	125.64
3629	88317	Inbound image	8.5	131.89
3631	88319	Inbound image	8.7	134.14
3638	88326	Inbound image	9.5	135.99
3643	88331	Inbound image	10.0	142.65
3645	88333	Inbound image	10.2	135.99
3650	88338	Inbound image	10.8	120.61
3652	88340	Inbound image	11.0	125.64
3659	88347	Inbound image	11.7	133.36
3666	88354	Inbound image	12.5	138.80
3671	88359	Inbound image	13.0	165.98
3673	88361	Inbound image	13.2	176.85
3678	88366	Inbound image	13.8	169.40
3680	89003	Inbound image	14.0	169.40
3694	89017	Inbound image	15.6	150.85
3699	89022	Inbound image	16.0	181.39
4055	90013	Periapsis image	17.1	221.84
4072	90030	Inbound image	8.0	241.14

In the YYDOY column, the first two digits are the year, and the last three digits are the day of the year.

*When the spacecraft-Venus vector intersects 30°N latitude (in hours).

Meier [1991] for an energy level diagram of the oxygen atom.)

Cascade to the $3s\ ^3S^0$ state primarily occurs via the 844.6-nm transition from the $3p\ ^3P$ state. This state is excited directly from the ground state by photoelectron impact and is also fed by cascade from $3d\ ^3D^0$ and $3s'\ ^3D^0$ states. The branching ratio for the 844.6-nm transition is

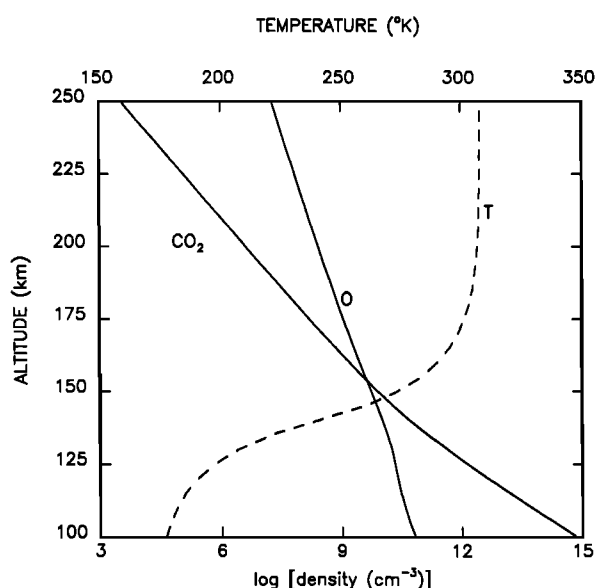


Fig. 2. Vertical profiles of temperature, O, and CO₂ used in the standard model developed in section 3. These profiles are derived from the VTS3 empirical model.

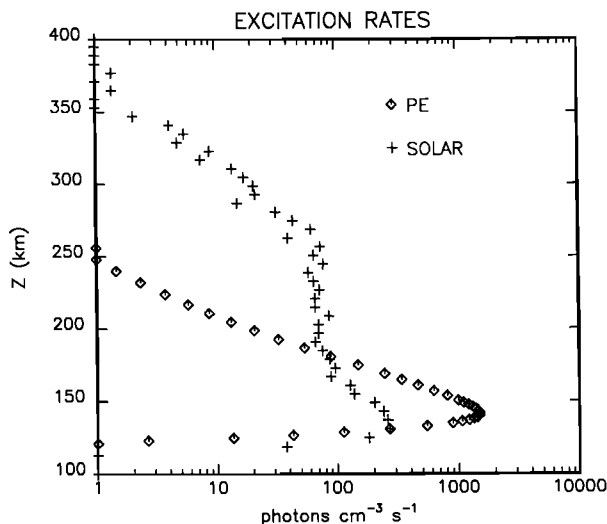


Fig. 3. Initial 130-nm excitation rates. Diamonds show the photoelectron impact excitation, and crosses show the solar resonance scattering excitation.

almost 100%. Branching for the $3d\ ^3D^0 \rightarrow 3p\ ^3P$ transition is smaller, $\sim 10\text{--}25\%$, but since the 102.7-nm photons are radiatively trapped in the atmosphere, much or all of the energy is funneled through the $3d\ ^3D^0 \rightarrow 3p\ ^3P \rightarrow 3s\ ^3S^0 \rightarrow 2p\ ^3P$ cascade. The $3s'\ ^3D^0 \rightarrow 3p\ ^3P$ transition has an even smaller branching ratio, $\sim 0.01\%$, but the 98.9-nm photons are also radiatively trapped, so the actual cascade will be enhanced above this value. A discussion of these branching ratios and their uncertainties can be found in Meier [1991]. Cascade can also occur via the $np\ ^3P$, $ns\ ^3S^0$, and $nd\ ^3D^0$ series ($n \geq 4$), but since excitation cross sections decrease with increasing transition energy, these are not important contributors to the 130-nm emission.

The PE excitation rates in our model are based on the work of Nagy and Banks [1970] and include the effects of vertical electron transport with a two-stream approximation. The Venus model is an adaptation of the terrestrial version described in Solomon et al. [1988] and Solomon and Abreu [1989]. The solar EUV irradiance is obtained by scaling the Hinteregger et al. [1981] SC 21REFW spectrum using the $F_{10.7}$ association method and two-class model. The spectrum is then normalized for the sun-Venus distance. The Torr et al. [1979; Torr and Torr, 1985] spectral intervals and selected lines are adopted. From this solar EUV and the appropriate Venus model atmosphere, photoionization rates and photoelectron production rates are computed as a function of energy and altitude. The energies considered range from 0.25 to 240 eV and are binned with an exponentially increasing energy bin size using the scheme of Swartz [1985]. Photoionization and dissociation cross sections are described in Torr et al. [1979] and Lawrence [1972], except for atomic oxygen which is taken from Samson and Pareek [1985]. Cross sections for electron energy loss processes are based on the work of Jackman et al. [1977] and Sawada et al. [1972a, b]. The 130-nm excitation rate is computed as the integral over energy of the product of the electron flux, excitation cross section and the number density of O.

The "direct" excitation cross sections of Doering and others [Doering and Vaughan, 1986; Vaughan and Doering,

1986, 1987, 1988; Gulcicek and Doering, 1988; Gulcicek et al., 1988] for O, are used to compute excitation rates to the $3s\ ^3S^0$, $3d\ ^3D^0$, $3s'\ ^3D^0$ and $3d\ ^3D^0$ states. Cascade contributions to the 130-nm emission are then computed by summing direct excitation to the $3s\ ^3S^0$, $3d\ ^3D^0$ and $3d\ ^3D^0$ states plus 10% of the direct excitation to the $3s'\ ^3D^0$ state. The total cascade contribution from these sources is equivalent to an enhancement of a factor of ~ 1.15 over the "optically thin" excitation rate which would result from using the Zipf and Erdman [1985] cross sections.

The resulting initial excitation rate for the photoelectron impact source is plotted as a function of altitude in Figure 3 (diamond symbols) for the subsolar, high solar activity ($F_{10.7} = 200$) case. The solar excitation rate, also plotted in Figure 3, is discussed in the next section.

3.2.2. Solar resonance scattering. The second most important source of O I 130-nm excitation (and the only other we consider) is resonance scattering of solar 130-nm photons by O atoms in the Venus thermosphere. The initial excitation rate for this mechanism, plotted with crosses in Figure 3, describes at what altitude the solar photons first scatter as they enter the atmosphere. The excitation for this source is quite broad in altitude with significant contributions from above the exobase at ~ 200 km. This excitation rate is derived from a Monte Carlo technique described in section 3.3.

The sun emits three broad lines at 130 nm from atomic oxygen in the solar chromosphere. Characteristic line widths are of the order of 2×10^{-2} nm corresponding to the high temperatures in the chromosphere ($\sim 10^4\text{--}10^5$ K). Compare this to the Doppler width for the 130-nm lines in the Venus thermosphere, which is about 2×10^{-4} nm. This means that the planetary scattering will be primarily only sensitive to the flux in the core of the solar lines. There are many difficulties associated with determining what this line-center flux is, so the excitation rate by this mechanism will be correspondingly uncertain.

The best measurements of absolute flux in the solar 130-nm triplet did not have the spectral resolution to resolve the line shapes [Mount and Rottman, 1985], and since the Mount and Rottman experiments were flown on short-lived rockets, they only tell us what the solar flux was on some particular day, and contain little information about how this flux varies with time. So we must couple these flux measurements to separate determinations of the line shapes, and of solar activity in order to predict the excitation. We have used the 130-nm measurements from the Solar Mesosphere Explorer (SME) satellite to describe the variation of the flux from the sun at this wavelength with solar activity, and the two rocket observations of May 17, 1982, and July 25, 1983, as calibration points for the SME data. With this procedure, we estimate a solar flux at 130 nm at the orbital distance of Venus to be 1.65×10^{10} photons $\text{cm}^{-2}\text{s}^{-1}$ for high solar activity (described by $F_{10.7} = 200$; see section 3.4.3). This value is only 60% of the value used in previous analyses of the PVOUVS measurements at 130 nm by Paxton and Meier [1986] and Meier et al. [1983], which assumed a flux of 2.7×10^{10} photons $\text{cm}^{-2}\text{s}^{-1}$ at Venus based on earlier rocket measurements [Mount and Rottman, 1981].

The line shapes for the three members of the 130-nm triplet are still highly uncertain. The shapes of the lines are known to vary from the center to limb of the sun, and most observations use a small aperture which observes only a

small fraction of the sun's surface at a time. The O scattering problem, on the other hand, will be sensitive to disc-averaged line profiles. The line shapes, and relative flux in each line, will also vary with time and solar activity, but it is not known how. Given these uncertainties, we chose a single line profile given by Bruner et al. [1970] and assume the total flux in the triplet is divided equally between the three lines. A recent analysis of 130-nm line profiles by the OSO-8 spectrometer [Gladstone, 1988] suggests somewhat narrower line profiles than that of Bruner et al., and uneven fluxes in the three lines. Adopting these line profiles would increase the emergent intensities in our model by amounts less than 10%, which is comparable to the effect the uncertainties in the absolute solar flux would have, and considerably smaller than the absolute uncertainty in the PVOUVS measurements to which we will be comparing this model.

3.3. Radiative Transfer

The radiative transfer technique used to solve the optically thick atomic oxygen 130-nm problem is the Monte Carlo method of R. R. Meier [Meier and Lee, 1982], adapted to Venus [Meier et al., 1983; Paxton and Meier, 1986], and modified from the original plane-parallel geometry to account for some of the important effects of spherical geometry on the observations. Contribution functions for nadir viewing geometry are plotted in Figure 4. These profiles describe at what altitude contributions to the emergent intensity originate. The integral over altitude of the contribution function gives the emergent column brightness. Compare these profiles to the excitation rates plotted in Figure 3. The peak of the contribution function occurs much higher, at ~ 155 km. The photons initially produced at the excitation peak (140 km) are highly radiatively trapped and tend to be either absorbed by CO₂ or scattered at a higher altitude before escaping out the top of the atmosphere.

This same Monte Carlo model has also been applied to Mariner 9 observations at 130 nm on Mars in Stewart et al. [1992]. Meier's Monte Carlo model has been tested against a variety of observations on Earth, Venus, and Mars, and further details of the method can be found in the sources referenced above. The modifications to account for the spherical geometry of the full disc PVOUVS observations are described below.

3.3.1. Modifications to the plane-parallel model. The need to modify the plane-parallel Monte Carlo model to account for spherical geometry is obvious from looking at the PVOUVS image data shown in Figure 1 and Plate 1. Clearly, the atmosphere lies above a spherical planet, not above a flat plane as the plane-parallel approximation assumes. The plane-parallel approximation works well for viewing angles and solar zenith angles less than $\sim 75^\circ$, but becomes increasingly invalid closer to the limb.

We include spherical geometry effects in the Monte Carlo radiative transfer model by modifying the incremental plane-parallel slant path,

$$ds = \sec \theta dz,$$

with a Chapman function relation,

$$ds = Ch(R, H_\tau, \theta) dz,$$

where θ is the angle from the vertical, R is the radial distance from the center of Venus, and H_τ is the "optical depth scale height," which is described by

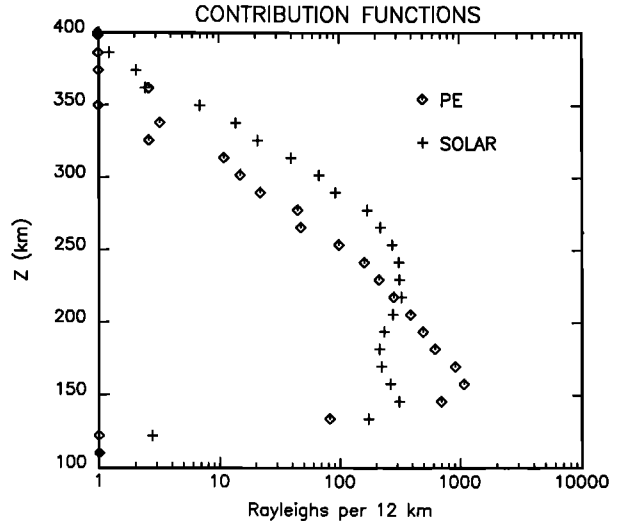


Fig. 4. Contributions to the emergent intensity in Rayleighs from each 12-km altitude interval. Diamonds show the photoelectron contribution, and crosses show the solar contribution.

$$H_\tau = \tau_v \left(\frac{d\tau_v}{dz} \right)^{-1}$$

τ_v is the vertical optical depth. Thus this Chapman function depends not only on θ and z , but also on frequency via τ_v .

The form of the Chapman function we use is an analytical approximation given by

$$Ch(R, H_\tau, \theta) = \sec \left(\theta - \frac{1}{y[1 + (y/\sqrt{4\pi})(\pi/2 - \theta)]} \right),$$

for $\theta \leq 90^\circ$, where

$$y = \sqrt{\pi R/(2H_\tau)}.$$

Use of this simple analytical form rather than a more exact numerical solution saves a tremendous amount of computing time because the slant path correction must be applied between every scattering within the Monte Carlo model. The spherical pathlength correction affects the model in three ways: (1) the optical depth at which incoming solar photons (external source) first scatter will be associated with a different altitude, (2) the change in optical depth for photons between scatterings will be associated with a different change in altitude, (3) the probability of escape (and subsequent detection) from a given altitude will be enhanced. The effects of points 1 and 3 are the most important. Figure 5 shows a comparison of limb brightening between the plane-parallel model and the spherical model. The difference is negligible at angles $\leq 70^\circ$, but the brightness is enhanced by 60% at 87° .

3.3.2. Radiative transfer model results. The altitude integral on the contribution function gives the value of the total column emission rate (in kilo-Rayleighs) for given atmospheric densities, temperature, and observational geometry. This total column brightness will be referred to as B_{130} . These model values can then be compared to measurements of column emission rate by the PVOUVS. It is not practical to model each data point in every PVOUVS image individually, especially because of the large amounts of

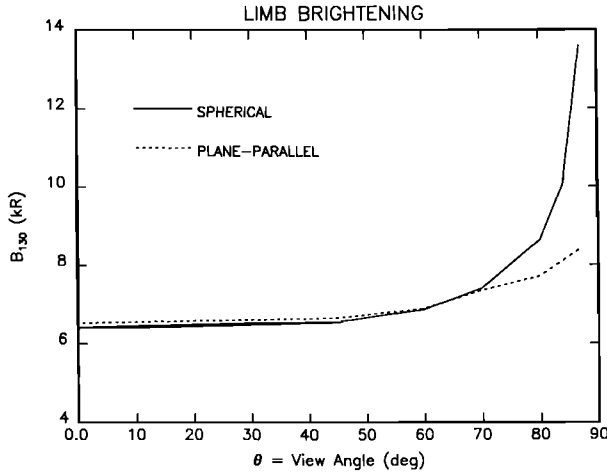


Fig. 5. Limb brightening differences between the plane-parallel and spherical model.

computing time consumed by the Monte Carlo radiative transfer method. We have created a suite of model calculations for appropriate ranges of O densities, solar zenith angles, and viewing angles. (The temperature profile is held constant throughout, as we have found it to have a negligible effect on the B_{130} .) These results then serve as reference tables from which we can interpolate to create synthetic images mimicking the data. Construction of the synthetic images is described in section 3.4. In this section we describe the results of the radiative transfer models which serve as the B_{130} reference tables.

We start with the standard set of vertical profiles for temperature, and O and CO₂ densities shown in Figure 2. These profiles come from the empirical VTS3 [Hedin et al., 1983] model of the Venus thermosphere. The standard model profiles correspond to the thermosphere at the subsolar point at a high solar activity index, $F_{10.7} = 200$. (The high solar activity case was chosen for the standard because it approximates conditions when the in situ measurements were made. The VTS3 profiles at low solar activity are more model dependent.) We first eliminated temperature as a variable in the radiative transfer problem by studying the effects of two extreme temperature profiles on B_{130} . The chosen profiles had exospheric temperatures of 308 K and 212 K, and represented the extremes of dayside temperatures expected at high and low solar activity. Temperature could potentially affect the radiative transfer by altering the shape of the scattering cross-section profile. Comparison of these two cases showed that the net effect of this extreme range of temperatures on B_{130} is less than 1%. Thus exospheric temperature variations are neglected in subsequent modeling, using only the profile shown in Figure 2. Solar activity can also affect B_{130} . Our method of accounting for changes in solar activity from day to day, and throughout the solar cycle, will be described in section 3.4.3.

Our radiative transfer model results are in Table 3. Three sets of calculations corresponding to different f_O (O mixing ratio at the 3-nbar pressure level) are given: $f_O = 17\%$, 12.75%, and 8.5%. We vary f_O in these models by multiplying the [O] profile in Figure 2 by a factor, constant in altitude. (This means we are not considering more subtle changes in the shape of the [O] profile in our standard model, but the column emission rate is rather insensitive to such

changes.) Photoelectron excitation rates are also scaled linearly with the O density, a valid assumption over the range of f_O we consider. These model results serve as reference tables in which we can interpolate to model the range of parameters (f_O , θ_0 , θ) covered by the PVOUVS observations.

3.4. Synthetic Image Construction

We construct synthetic images for comparison to the data by combining the known geometry of each PVOUVS image with the radiative transfer results described above. Examples of the finished product are shown in Figure 6. These synthetic images incorporate our previous knowledge about the general structure of the Venus thermosphere. In section 4, we will use the comparison of these synthetic images to the data images to infer anomalous patterns in thermospheric atomic oxygen.

3.4.1. Description of the technique. The known geometry associated with each scan of the PVOUVS line of sight across the planet is used to compute a point-by-point model prediction of the column brightness. To create a synthetic image, we compute θ and θ_0 , at each point, from this known geometry, pick a value of f_O , then do a three-way interpolation in (θ, θ_0, f_O) space within the reference tables (Table 3). These model predictions are then rectified in the same way as the data to create the synthetic images like those in Figure 6.

Our point-by-point modeling includes the effects of slit-smear and spin motion compensation. We model five equally spaced points along the long axis of the slit and average them rather than modeling only the slit center geometry. We also model three points in time within each 8-ms integration period. The spin of the spacecraft results in changing line-of-sight geometry during that period. By averaging all of these modeled points, we get a more realistic prediction of the actual measurements.

3.4.2. Dayside distribution in f_O . The last parameter which must be specified before assembling the synthetic images is f_O (the oxygen mixing ratio at the altitude of the

TABLE 3. The 130-nm Column Brightness in Kilo-Rayleighs

θ_0 , deg	θ , deg						
	0	45	60	70	80	84	87
$f_O = 17.0\%$							
0	8.77	8.90	9.23	9.84	11.24	13.30	17.90
45	7.65	7.73	8.05	8.65	9.96	11.56	15.61
60	6.39	6.56	6.87	7.40	8.63	10.05	13.59
70	5.09	5.46	5.72	6.18	7.25	8.62	11.87
80	3.65	3.83	4.03	4.40	5.26	6.35	8.95
$f_O = 12.75\%$							
0	7.08	7.14	7.36	7.86	8.93	10.51	14.21
45	5.90	6.23	6.50	7.01	8.18	9.42	12.74
60	4.93	5.24	5.48	5.93	6.96	8.27	11.38
70	4.08	4.32	4.54	4.94	5.86	6.96	9.67
80	2.90	3.01	3.18	3.49	4.23	5.15	7.33
$f_O = 8.5\%$							
0	5.52	5.67	5.83	6.23	7.12	8.45	11.45
45	4.62	4.80	4.98	5.37	6.28	7.29	9.97
60	3.83	4.05	4.25	4.62	5.47	6.56	9.12
70	3.08	3.34	3.52	3.84	4.60	5.59	7.86
80	2.10	2.25	2.36	2.59	3.14	3.91	5.65

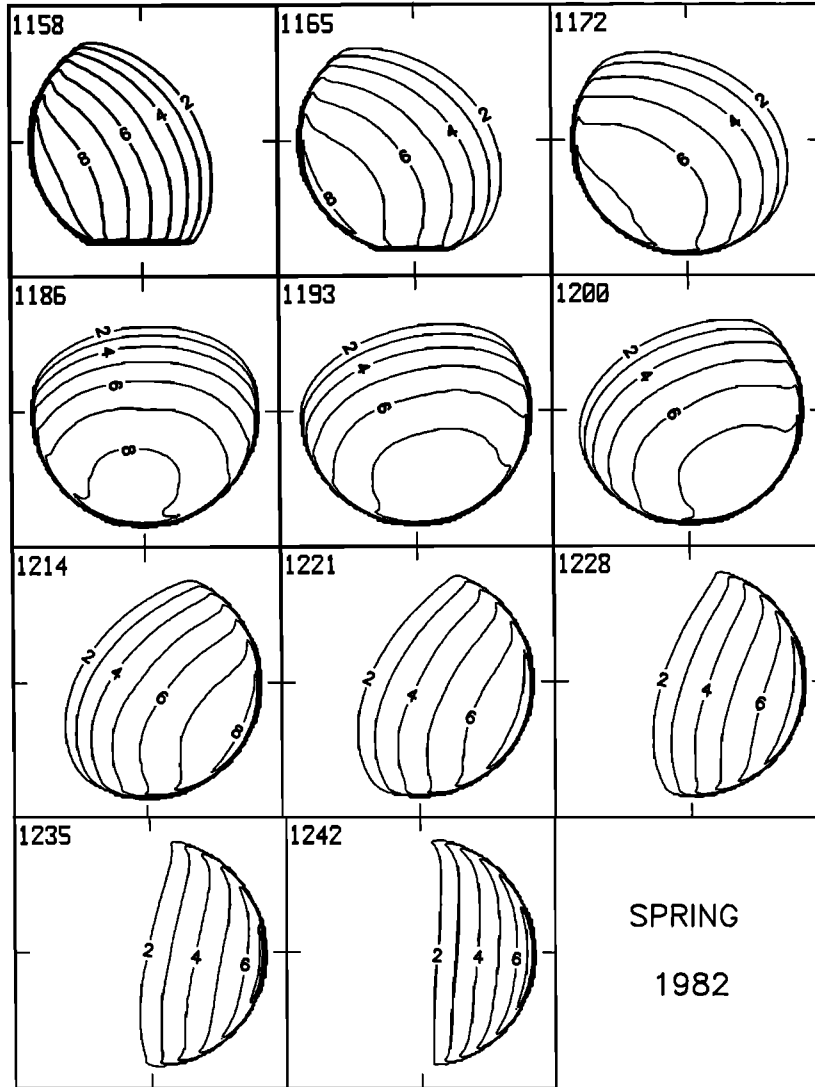


Fig. 6. Synthetic images for the same orbit series shown in Plate 1. Contours are in kilo-Rayleighs.

B_{130} source peak), and its distribution across the dayside as a function of latitude and local time. To test the sensitivity of our model to the f_O distribution, we first tried to fit the data with a constant dayside f_O . The 8.5% model fit the terminator region but was 30% too low at the subsolar point. The 17% model, on the other hand, fit the subsolar values but was a factor of 2 too large at the terminator. A gradient in f_O as a function of solar zenith angle (θ_0) was needed to recreate the average trends seen in the data. For our standard model, we choose a distribution which is very similar to the VTGCM results, but we ignore the small asymmetries about the subsolar point, and represent it with an analytical form,

$$f_O = 15\% \times \mu_0^{1/3}$$

This distribution approximates the VTGCM distribution to within $\sim 10\%$ for all $\theta_0 \leq 80^\circ$. It gives a good fit to the general trends observed in the data, within the constraint of a purely solar zenith angle dependence. The choice of this simple pattern is in accord with theory, and will simplify the interpretation of the results in section 4.

3.4.3. Solar activity corrections. To account for variations in solar activity, we utilize the results of *Brace et al.*

[1988] and the proxy indicator they call $VF_{10.7}$. $VF_{10.7}$ is analogous to the $F_{10.7}$ index used to describe solar activity at Earth, which is the value of the solar radio flux at 10.7-cm wavelength at 1 AU in units of $10^{-22} \text{ W m}^{-2} \text{ Hz}^{-1}$. $VF_{10.7}$ is, however, derived from measurements by the Langmuir probe instrument on board the Pioneer Venus Orbiter and has no direct relation to the solar 10.7-cm flux. When the orbiter is outside of the Venus atmosphere, the flux from the sun at ionizing EUV wavelengths generates a photoelectron current in the Langmuir probe, i_{pe} . *Brace et al.* estimate that 51% of the current is contributed by the flux at Lyman α (121.6 nm) and 46% by shorter wavelengths between 50 and 110 nm (and 3% from longer wavelengths). Thus $VF_{10.7}$ is an ideal indicator of solar activity because these solar emissions are very similar to the excitation sources for the O I 130-nm problem. In addition, $VF_{10.7}$ is a better proxy than other solar activity indicators measured on the Earth because the Langmuir probe is orbiting Venus along with the PVOUVS. No corrections for solar rotation variations in activity are necessary.

Figure 7 shows a correlation between $VF_{10.7}$ and daily "brightness factors" for the O I 130-nm emission from

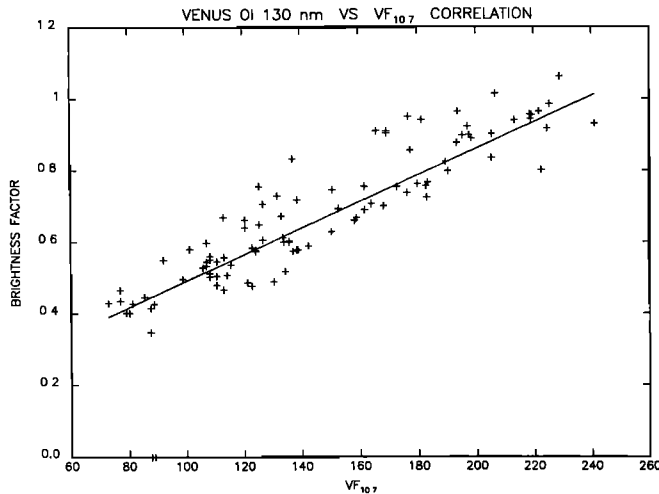


Fig. 7. Correlation between $\text{VF}_{10.7}$ solar activity indicator and brightness factor for each 130-nm image. The straight line is the weighted least squares fit.

Venus. The data in this plot span a 10-year period, 1980–1990. The brightness factor is an image-averaged ratio of data and synthetic image. Data images and synthetic images are first ratioed to normalize the observations for changing geometry (phase angle) from day to day. The brightness factor is then the weighted average of the ratio image. Since the standard model used in creating the synthetic images is based on a high solar activity ($\text{VF}_{10.7} = 200$), most of the brightness factors are less than or equal to unity. A weighted least squares fit to the correlation in Figure 7 is plotted as a straight line and is described by

$$\text{brightness factor} = 0.004(\text{VF}_{10.7} + 25)$$

We utilize this correlation in correcting the synthetic images for variations in solar activity by defining an “activity factor,”

$$A = \frac{0.004(\text{VF}_{10.7} + 25)}{0.004(200 + 25)}$$

The synthetic images are then multiplied by their appropriate activity factor to approximate solar activity effects on the overall brightness.

It is worth noting that this solar activity correlation is a blend of two effects: (1) variations in the flux of the exciting solar radiation, and (2) variations in atomic oxygen densities with solar activity. The O density will vary with solar activity because ultimately the source for O is photodissociation of CO_2 . We do not try to separate these two effects because it will change neither the synthetic B_{130} images, nor the conclusions derived from them. However, such a study could potentially yield important information on the variation of O with solar activity, providing a test for modelers, because all of the in situ data have been obtained during periods of high solar activity.

4. MODEL COMPARISONS TO THE 130-NM DATA

Some of the apparent structure in the 130-nm images is predicted by our model, specifically the limb brightening and the subsolar-to-terminator darkening. By taking the ratio of these data to the synthetic images, the anomalies can be

clearly seen. An interesting pattern emerges, previously obscured by subsolar-to-terminator darkening, which will be the focus of this paper.

Plate 2 shows a series of these ratio images for the same set of data as shown in Plate 1. The color scale refers to the value of the ratio of the column emission rates, data over model. This ratio will be referred to as R_{130} . The bright features which were apparent in the 130-nm images in the subsolar region still appear and can now in some cases be traced further into the terminator region (e.g., orbit 1165). In addition, a high-contrast feature appears in each image at the high latitudes as a dim patch near the morning (right) terminator and relatively bright area along the evening (left) terminator. These brightness anomalies can be related directly to anomalies in the atomic oxygen density since all the other variables are either known or have been eliminated. Using f_O (oxygen mixing ratio at 3 nbars) to characterize the oxygen density, the relationship between B_{130} and f_O can be inferred from the model results in Table 3. The relationship is approximately linear over the range in f_O considered for Venus. ΔB_{130} will be used to describe the percent change in brightness from the standard model seen as highs and lows in the ratio images: $\Delta B_{130} = (R_{130} - 1) \times 100\%$. So a value of brightness ratio $R_{130} = 1.2$ corresponds to $\Delta B_{130} = 20\%$, and a ratio of 0.8 corresponds to $\Delta B_{130} = -20\%$. Similarly Δf_O will be used to describe percent variations in oxygen mixing ratio from the standard model.

4.1. Description of Brightness Anomalies

The anomalous features in B_{130} or f_O can be classified into two main types: (1) “transient” features which come and go and change in form from image to image, and (2) “solar-locked” features, which are persistent patterns, stationary in a solar-locked frame (i.e., local solar time and solar latitude).

4.1.1. Transient features. The transient features observable in the PVOUVS images have large horizontal scales, of the order of 1000 km or greater. Some of these features are linearly organized as bands along a line of constant latitude, or at some angle. Others are more rounded or irregularly shaped. These features typically have brightness variations $\Delta B_{130} \sim +25$ to -30% , although some of these features vary by as much as $\pm 50\%$. (Note that statistical noise in these images corresponds to a standard deviation of only $\sim 5\%$.) These brightness variations correspond to variations in oxygen density Δf_O of typically $\sim \pm 40\%$, and occasionally as much as 80%. At the nominal frequency of PVOUVS 130-nm image acquisition of 1 week, these transient features either disappear and reappear, or change in form; we do not have the temporal resolution to distinguish the two. They probably persist for at least a matter of hours (because it takes 1.5–3 hours to assemble one of the PVOUVS images) and probably dissipate or change in form on a time scale less than a few days. Although these features are referred to as transient because they change in form and location, there is structure of this type in every image analyzed in this manner; 64 in all, spanning 10 years, and at both high and low solar activity. The present paper does not attempt to explain these interesting anomalies, but instead focuses on the persistent solar-locked features.

4.1.2. Solar-locked features. The second type of brightness anomaly observed is locked in local solar time and solar latitude. The most obvious of these features can be

observed in the northern hemisphere in the inbound ratio images (Plate 2). The morning (right) and evening (left) terminators can serve as local time reference points. The solar-locked pattern appears as a consistently dark patch (blue) in the early morning hours and relatively bright region (yellow to red) in the late afternoon hours along the evening terminator. These are stable features which may vary in intensity from day to day but are virtually always present. The pattern can best be described as an asymmetry in local time, with afternoon hours much brighter (more O) than corresponding morning times. Close to the terminator, the afternoon $\Delta B_{130} = 0$ to $+50\%$ ($\Delta f_O = 0$ to $+80\%$), while near the morning terminator $\Delta B_{130} = -20$ to -60% ($\Delta f_O = -30$ to -75%). This asymmetry in neutral oxygen has never previously been observed, since the PVONMS measurements did not extend to latitudes north of 30° , and atmospheric probes have consistently entered only in the morning hemisphere. (Veneras 11 and 12 entered shortly after 12 noon, but near the equator.) In the following sections, the average properties of this feature are characterized, and its temporal stability examined.

4.2. Long-Term Average Maps

To examine the average properties of the solar-locked features in B_{130} , each ratio image is first mapped into local solar time and latitude. These individual maps are then averaged into one grand average map. The data have been organized into two separate groups: one for inbound images and one for periapsis images because of their very different spatial resolutions and local time coverages. The periapsis data contain fewer measurements but allow examination of latitudes south of 30°S . The results are shown in Figures 8a and 8b. These maps show average values of the brightness ratio R_{130} as a function of local time and latitude. They have been smoothed for clarity of presentation.

The inbound image results are in Figure 8a. The local time asymmetry stands out clearly at latitudes north of 30° . At equatorial latitudes the local time variation is much more subtle. A shallow low appears centered about 1400–1500 hours local time. A similar feature was observed at higher altitudes by the PVONMS [Niemann et al., 1980]; however, the PVONMS result could not be distinguished from possible 28-day solar activity variations [Hedin et al., 1983]. Our result indicates that this minimum in f_O is real and stable. (It can also be seen in the periapsis data (Figure 8b) and in the VTS3 comparison in Figure 10b.)

The periapsis map is shown in Figure 8b. There is a factor of 4 fewer data in this map compared to Figure 8a, but the high spatial resolution associated with these measurements allows us to more clearly examine the southerly latitudes. In this map we can begin to see the local time asymmetry emerging in the southern hemisphere just as in the north. We conclude that there are no obvious north-south hemispheric asymmetries in this solar-locked pattern.

In summary, the appearance of the long-term average solar-locked feature is characterized by an asymmetrical trend with local time resulting in a $\Delta B_{130} = 0\%$ ($\Delta f_O = 0\%$) at the evening terminator, and a minimum $\Delta B_{130} = -45\%$ ($\Delta f_O = -60\%$) near the morning terminator. This variation in brightness ratio is associated with up to a factor of 2.5 variation in f_O from morning to evening, where only a 10% variation is predicted by the VTGCM. The pattern emerges

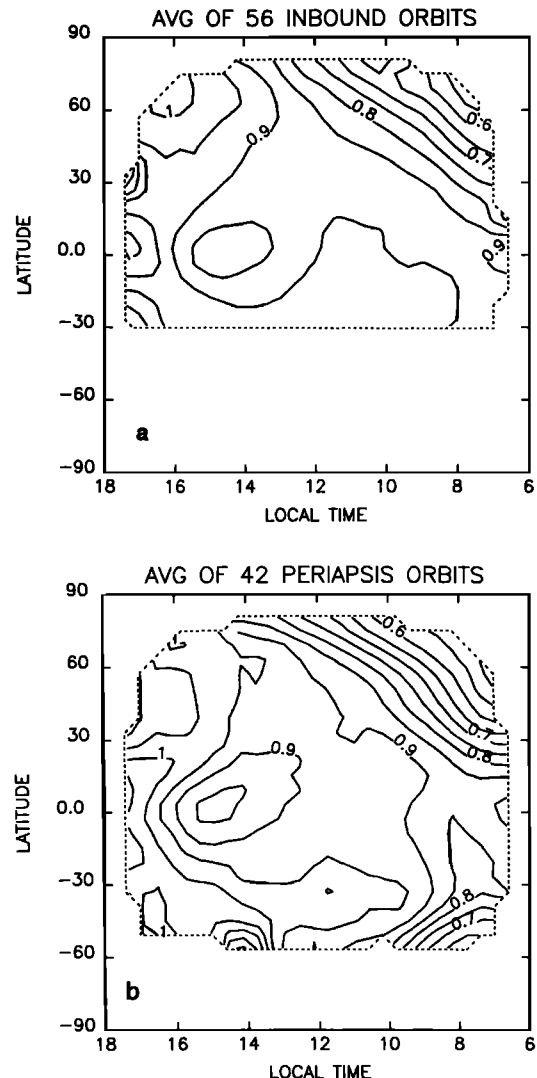


Fig. 8. Contours of brightness ratio mapped into local solar time and solar latitude. These are long-term averages including the entire set of observations in Table 2. (a) Average of inbound image data. (b) Average of periapsis image data.

at latitudes poleward of 30° with no apparent north-south hemispheric asymmetry.

4.3. Temporal Stability of the Local Time Asymmetry

To examine the temporal stability of this solar-locked feature, the dayside observations north of 30°N latitude are divided into three sectors in local solar time: 0600–1000, 1000–1400, and 1400–1800. For each 130-nm image, the average value of R_{130} is computed for each of these sectors. These sector-averaged R_{130} are plotted in Figure 9 on an orbit-by-orbit basis. Triangles represent the late afternoon values, noon sectors are plotted as diamonds, and squares represent the early morning sectors. Note that each sector may not be equally represented in a given image because of the variable phase angle from image to image. However on most orbits, in fact, in every case where we have a reasonably clear view of all three sectors, late afternoon sectors are brighter than their corresponding morning sectors. Noon-centered sectors are intermediate in value. The absolute values may change in time, but the pattern persistently

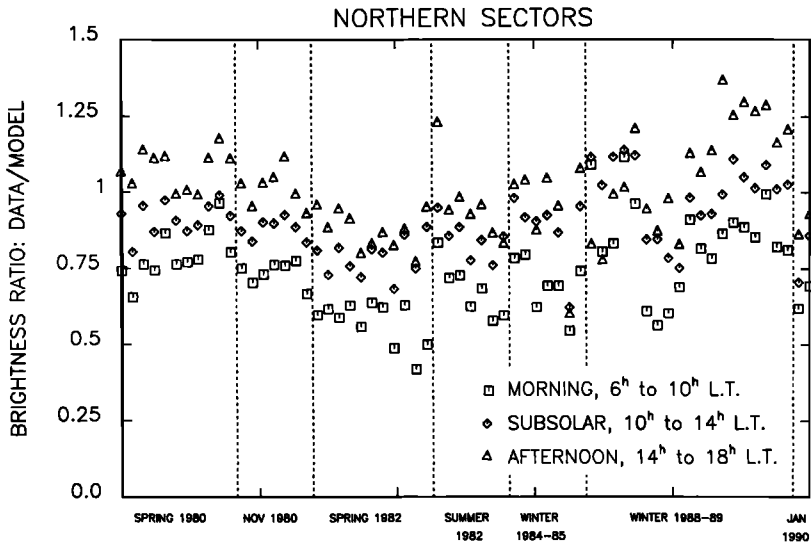


Fig. 9. Results of the sector analysis for latitudes north of 30° . Late afternoon sectors (triangles) are consistently brighter than corresponding morning sectors (squares).

remains. This is a remarkable result considering the length of time covered by these observations. They span a 10-year period, almost a complete 11-year solar activity cycle. Clearly, this solar-locked pattern of local time asymmetry is telling us about some very persistent and stable process organizing the large-scale structure of the thermosphere. In section 5 this will be explored further, and a dynamic mechanism will be proposed which can explain many of the key features of this result in the context of the thermospheric general circulation pattern.

4.4. Comparisons to Other Models

In order to put the results presented in Figure 8 into perspective, we compare our standard model to two other global models of the Venus thermosphere: the VTGCM and the VTS3. Predictions of global brightness patterns are prepared using each of these two models as input. A ratio of these brightness predictions to the standard model can then be compared directly to the data/standard model ratio shown in Figure 8. Since the standard model is purely symmetric about the subsolar point, it is interesting to compare to the VTGCM with its prescribed superrotation and to the VTS3 with its empirically based structure.

4.4.1. VTGCM comparison. Figure 10a shows a map of R_{130} derived from VTGCM densities, much like the data/model comparison in Figure 8. Here, the VTGCM-based column emission rate has been ratioed to the standard model. Comparing Figure 10a to Figures 8a and 8b gives a picture of how the VTGCM predictions compare to the PVOUVS observations. The average value of the ratio in this map is ~ 0.8 compared to the data maps (Figure 8), which have an average value of about 0.9. Thus if the absolute calibration of the PVOUVS were perfect, the 130-nm data would suggest that oxygen densities in the thermosphere are intermediate between the VTGCM and the standard model. Subsolar values of f_0 are 10% in the VTGCM and 15% in the standard model. However, since the absolute calibration of the PVOUVS is good to only $\pm 20\%$, a firm value cannot be placed on the absolute oxygen densities with these results.

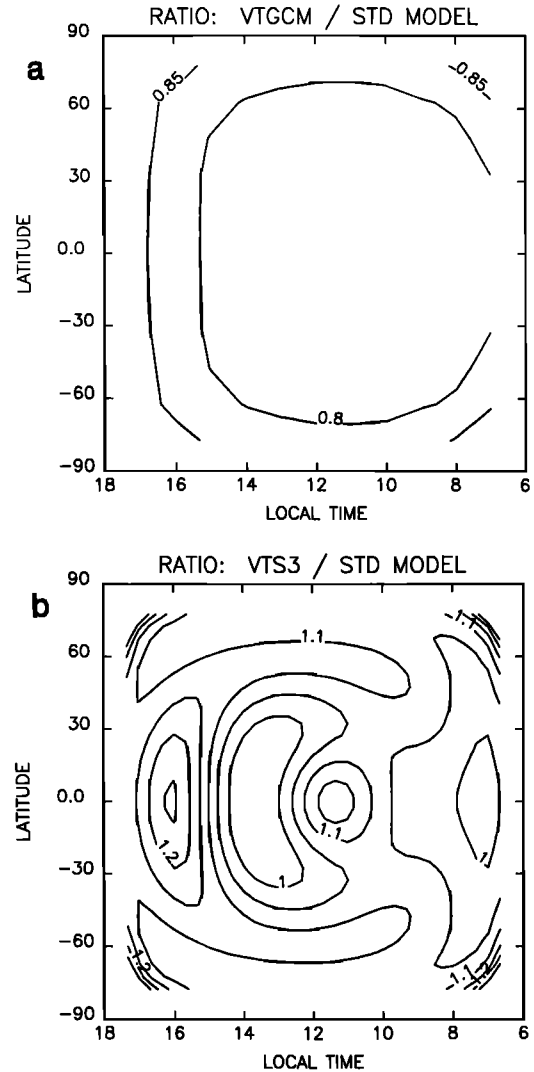


Fig. 10. Comparison of two global thermospheric models to the standard model developed in section 3. (a) VTGCM comparison. (b) VTS3 comparison. These patterns should be compared to the data/standard model comparison in Figure 8.

The VTGCM densities are also slightly asymmetric in local solar time in comparison to the standard. The small VTGCM asymmetry is a result of the asymmetric drag forces introduced into the VTGCM to reproduce the superrotation component of the wind field. The VTGCM's f_0 asymmetry of $\sim 10\%$ produces only a little over a 5% asymmetry in B_{130} , much smaller than what is observed in the data.

4.4.2. VTS3 comparison. Figure 10b shows the same comparison of column brightness for the VTS3 empirical model thermosphere. The map presents brightnesses predicted from VTS3 densities in ratio to the standard model brightnesses. The VTS3's f_0 values are somewhat higher than the standard model, but this comparison cannot definitively say the VTS3 atomic oxygen densities are too high, again because of the PVOUVS calibration uncertainty.

As noted earlier, the VTS3 does capture the local minimum observed near 1400–1500 at low latitudes, where the VTS3 is based on actual measurements. Comparing Figures 8 and 10b, the pattern in local solar time near the equator is similar, and the differences in magnitude are mostly within the uncertainties in the PVOUVS calibration. Difficulties arise when the VTS3 extrapolates the PVONMS results to other latitudes using spherical harmonic fits. The VTS3 shows structure not present in the data and misses the striking high-latitude patterns completely. Thus the VTS3 should be used with caution at extratropical latitudes poleward of 30° and is not a reliable predictor of latitudinal variations in atomic oxygen.

5. IMPLICATIONS FOR THERMOSPHERIC STRUCTURE AND DYNAMICS

5.1. Oxygen Time Scales

In order to explain the persistent solar-locked patterns in brightness observed in the 130-nm images, a mechanism for altering the atomic oxygen density locally in latitude and local time must be identified. What processes are important for determining the oxygen density? Which might vary in a latitude/local time frame, and why? To begin to answer these questions, we compare time scales for various thermospheric physical processes controlling the oxygen density.

On the dayside, the important physical processes are (1) production of O by photodissociation of CO₂ and by ion chemical reactions, (2) chemical loss, primarily via O + O + CO₂ \rightarrow O₂ + CO₂, (3) molecular diffusion, (4) eddy diffusion, and (5) vertical advection. In Figures 11a and 11b the time scales for these processes are plotted as functions of altitude, using the results of the VTGCM near the subsolar point (noon, 2.5°N). The primary source of O on the dayside is photodissociation of CO₂, which occurs rapidly over a wide range of altitudes. Chemical losses of O are only beginning to become important at the lower boundary of the thermosphere. Eddy diffusion is the process which can mix O downward from thermospheric source regions to lower altitudes, where chemistry can begin to act to remove it. Vertical advection on the dayside acts to transport O upward in altitude. Horizontal advection is less important over the length scale of interest (except in regions very close to the terminator) because the horizontal gradient in O is so much smaller than the vertical. Molecular diffusion is unimportant in the critical lower thermosphere region.

Since the process with the shortest time scale at a given altitude will dominate, O in the upper thermosphere is

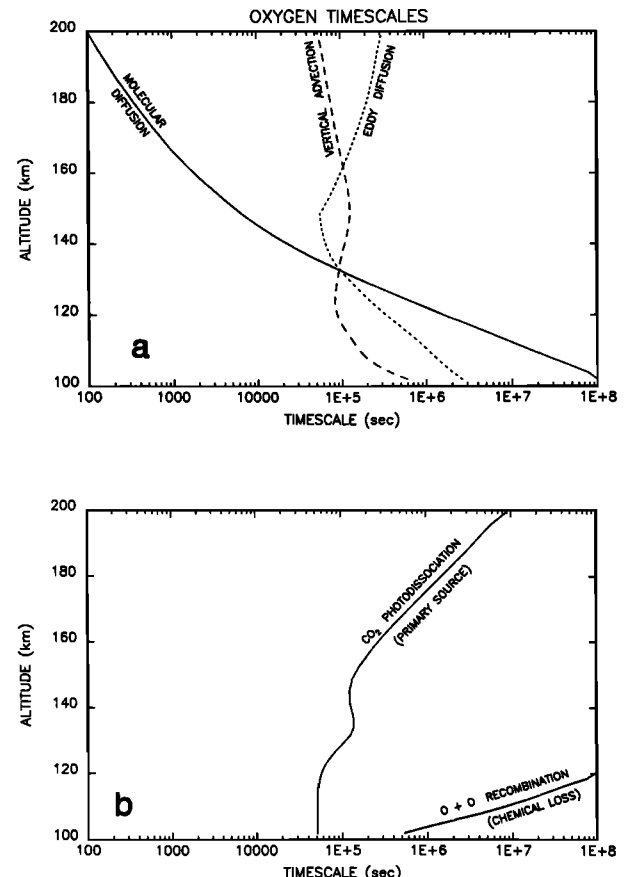


Fig. 11. Time scales for processes affecting the atomic oxygen density at the subsolar point.

controlled by molecular diffusion. The time scale for molecular diffusion above 140 km is only a few hours or less, so changes in the oxygen density sustained in the middle thermosphere can be rapidly communicated to the higher altitudes via this mechanism. In the lower thermosphere, advection is the primary transport mechanism for O. Eddy diffusion is not a dominant player at any altitude in the VTGCM. But if the eddy diffusion coefficient were larger by an order of magnitude, say, at certain latitudes and local times, it would become the dominant process in the middle and lower thermosphere, transporting O from the thermospheric source toward the lower boundary, where chemistry can act to consume it. Larger eddy diffusion coefficients should thus lower thermospheric O, and such a change in the middle and lower thermosphere could be rapidly communicated to the upper thermosphere via the process of molecular diffusion. Conversely, much smaller eddy diffusion coefficients would give advection and molecular diffusion complete control of oxygen transport, and thermospheric O would tend to increase until some new equilibrium is established. Thus local variations in eddy diffusion due to localized differences in wave breaking activity might explain the variations in O observed in the PVOUVS 130-nm data. In the next section, eddy diffusion effects are examined in a more quantitative fashion via experiments with the VTGCM.

5.2. Eddy Diffusion Effects on Oxygen

In the three-dimensional VTGCM, large-scale advection is treated explicitly. However, eddy diffusion is still used to

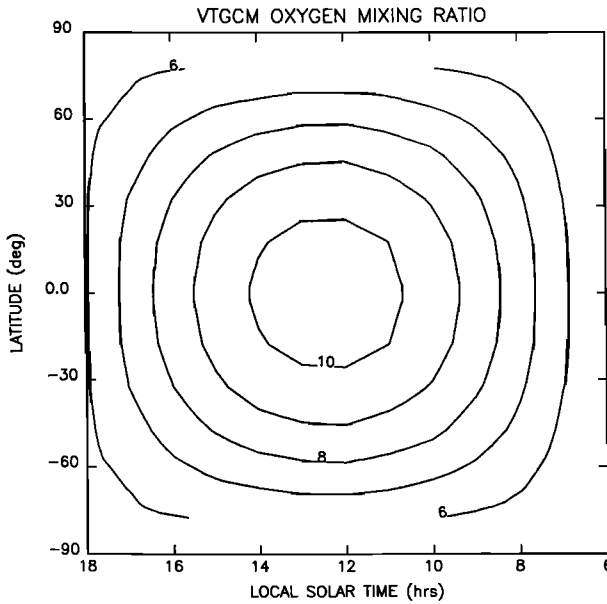


Fig. 12. The f_O distribution for the dayside from the VTGCM. This is the unperturbed model result for comparison to Figures 13–15.

parameterize turbulent mixing processes on scales smaller than the VTGCM grid scale. (The horizontal resolution of the VTGCM is 20 min of local time \times 5° latitude, and the vertical resolution is approximately $\frac{1}{2}$ scale height.) Values of the eddy diffusion coefficient K are in general much smaller than values used in corresponding one-dimensional models which try to describe both the large-scale advection and small-scale mixing with the same diffusion parameterization. The upper limit on global average eddy diffusion in the VTGCM has been determined to be $2 \times 10^7 \text{ cm}^2 \text{ s}^{-1}$ [Bougher et al., 1990] using observed NO nightglow intensities as a constraint. Compare this to the $5 \times 10^8 \text{ cm}^2 \text{ s}^{-1}$ value in the one-dimensional model in von Zahn et al. [1980]. This difference between one- and three-dimensional models can give very different results for the profile of O in the lower thermosphere, where advection is most important. In addition, the three-dimensional model responds very differently to changes in the eddy diffusion coefficient; one-dimensional models are much more sensitive to the parameter. For these reasons the VTGCM is used to quantify the effects of variations in eddy diffusion.

In the current VTGCM, eddy diffusion is given a vertical profile similar to that in von Zahn et al. [1980], specifically,

$$K(z) = K_t \left(\frac{p_0}{p(z)} \right)^{1/2} \quad p > p_0$$

$$K(z) = K_t \quad p \leq p_0$$

where $p(z)$ is pressure, $p_0 = 5$ nbars, $K_t = 1 \times 10^7 \text{ cm}^2 \text{ s}^{-1}$, and K_t is constant across the dayside hemisphere [Bougher et al., 1988]. We test the effect of local changes in K by modifying the profile with a multiplicative factor, constant in z , but varying in latitude (λ) and local solar time (t in hours):

$$K(z, \lambda, t) = K(z) C(\lambda, t)$$

where $C(\lambda, t)$ defines the latitude and local time distribution of the multiplicative factor to be specified.

Two simple configurations of $C(\lambda, t)$ were chosen for this study. One is a band parallel to lines of constant latitude, which is constant in local time but varies with a Gaussian profile in latitude. It is centered about the lowest latitude value in the VTGCM at 2.5° and has a Gaussian full width at half maximum (FWHM) of 20°. The second configuration is a circular patch with a Gaussian distribution in latitude and local time centered about 0900 and 47.5°, again with a FWHM of 20° of latitude/longitude. The peak magnitude of the factor $C(\lambda, t)$ will be varied from zero to 8. When these eddy diffusion configurations are inserted into the VTGCM, they perturb the pattern of the oxygen distribution. The normal pattern of f_O in the VTGCM is shown in Figure 12 and should be used as a reference in comparison to the new perturbed patterns.

Figure 13 shows the pattern of f_O derived by enhancing eddy diffusion by a factor of 4 in a band at the equator. Oxygen densities are reduced by 35–40% at the equator, and the effect gradually dies out at higher latitudes away from the perturbation. The corresponding brightness perturbation for this case would reach a maximum of –20 to –25% at the equator.

In the next case, shown in Figure 14, eddy diffusion is perturbed by up to a factor of 8 in a spot centered at 0900 and at mid-latitudes. In this case the oxygen perturbation reaches –40 to –45%, and the corresponding 130-nm brightness perturbation will exceed –25%. It is interesting to note the wake of the oxygen perturbation downwind of the eddy diffusion perturbation in Figure 14, but the effects of these localized changes in eddy diffusion still remain largely confined to the region surrounding the perturbation.

In a third simulation (Figure 15) the eddy diffusion coefficient was allowed to drop off to zero in a band centered at the equator. In this case, the oxygen density increases. Figure 15 shows f_O is 25–30% higher at the equator than the unperturbed model shown in Figure 12. The corresponding

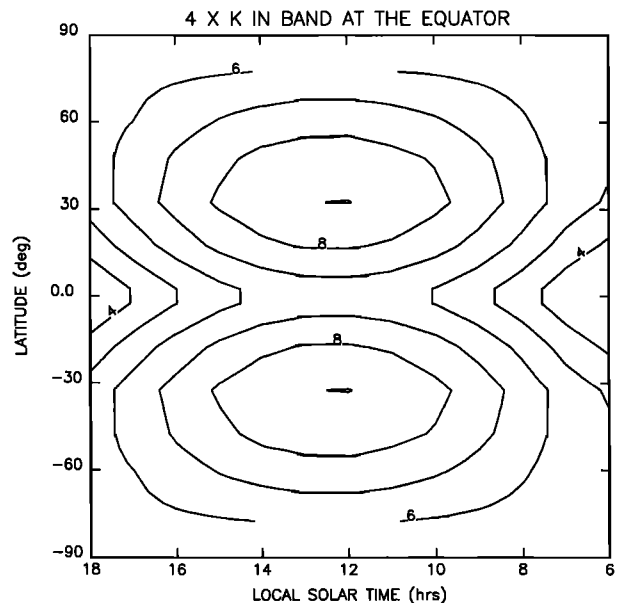


Fig. 13. Results of the VTGCM test with eddy diffusion enhanced by a factor of 4 in a band at the equator. The f_O (O-mixing ratio at 3 nbars) contour map is shown. Oxygen is depleted by up to 35–40%.

enhancement in 130-nm brightness in this case will be 15–20% in the vicinity of the perturbation.

These simulations demonstrate that localized variations in eddy diffusion could provide the explanation for the anomalous patterns in brightness observed in the PVOUVS 130-nm data. Variations in eddy diffusion ranging from very small values to values 8 times larger than those currently in the VTGCM can reproduce the typical range of observed brightness anomalies. Looking again at the long-term average map displaying the solar-locked brightness anomalies (Figure 8), this hypothesis suggests a local time variation in eddy diffusion at latitudes poleward of 30°. The pattern suggests that eddy diffusion decreases steadily as a function of local time with maximum values at the morning terminator, and minimum values at the evening terminator. The physical mechanism behind this eddy diffusion is presumably turbulent mixing generated by breaking gravity waves at thermospheric altitudes. This mechanism and an explanation for the local time asymmetry is explored in the following section.

5.3. Gravity Wave Saturation and the Lindzen Parameterization

The PVOUVS 130-nm images contain evidence for latitude and local time variations in turbulent mixing in the Venus thermosphere. The observational evidence supporting the presence of internal gravity waves, and their effects on the thermosphere are discussed by Alexander [1992]. Such waves can transport energy and momentum vertically from the lower to the upper atmosphere and can have a profound impact on the thermosphere. In the absence of dissipation, gravity waves will grow in amplitude as they propagate upward through the exponentially decreasing atmospheric density. Gravity wave saturation processes are those which act to limit or reverse this growth in amplitude via wave instabilities [Fritts, 1984]. Here, the term “satura-

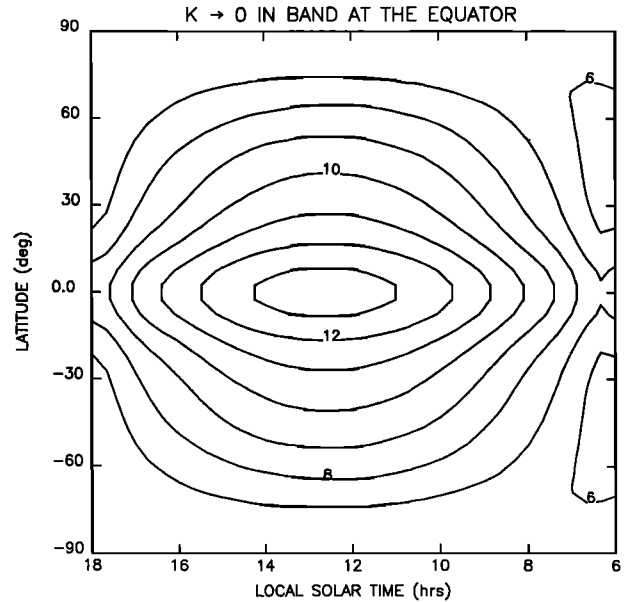


Fig. 15. Same as in Figure 13, but with eddy diffusion depleted in a band at the equator. Oxygen is enhanced by 25–30%.

tion process” refers to turbulent mixing (or eddy diffusion) and momentum deposition (or mean flow acceleration). In this section, it is shown that the wave source hypothesis, developed by Alexander [1992] to explain the thermospheric superrotation, can also provide an understanding of the local time asymmetries in the 130-nm brightness observed by the PVOUVS. The Lindzen [1981] parameterization is used to demonstrate local time variations in eddy diffusion which arise from the cloud-level wave interaction with the large-scale SS–AS thermospheric circulation.

Lindzen [1981] developed a parameterization for the effects of gravity wave saturation processes in terms of the mean state of the atmosphere and the characteristics of a monochromatic wave source. He described eddy diffusion and wave-induced acceleration above the wave-breaking altitude, z_b . The amplitude of a gravity wave will grow exponentially in the absence of dissipation to conserve energy as it propagates vertically. At some altitude, called the breaking level, the amplitude will exceed the stability limits of the atmosphere. Above z_b , Lindzen then assumed that the wave remains just saturated (deposits just enough of its energy to maintain a constant amplitude with height). With these simple assumptions, the breaking level is a function of the mean state of the atmosphere as well as the initial amplitude and altitude of the source. For the problem considered here, we can only speculate about the source, so the breaking level will be arbitrarily chosen.

Above z_b , eddy diffusion is described as an energy loss term in the linearized thermodynamic equation for the wave. Assuming that the wave growth is just balanced by this eddy diffusion term, Holton [1982], following Lindzen’s method, derives

$$K = \frac{k(\bar{u} - c)^4}{N^3} \left[\frac{1}{2H} - \frac{3}{2} \left(\frac{1}{\bar{u} - c} \frac{d\bar{u}}{dz} \right) \right] \quad (1)$$

for a zonally propagating wave with horizontal wavenumber k and phase speed c in a mean zonal wind \bar{u} . H is the scale

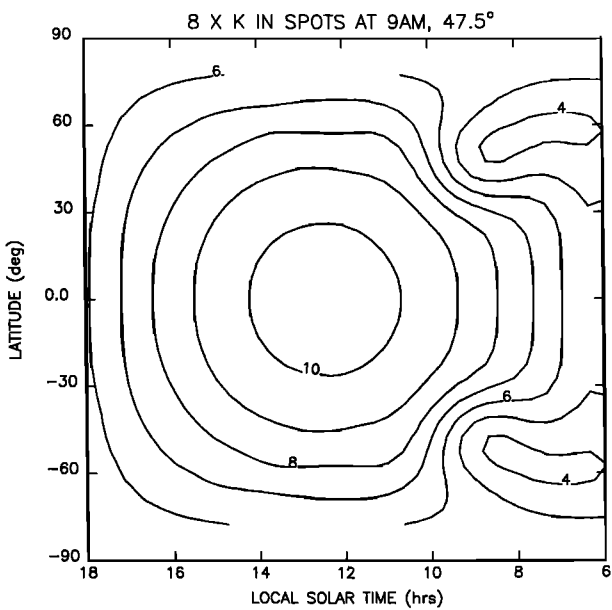


Fig. 14. Results of the VTGCM test with eddy diffusion enhanced by a factor of 8 in a spot at 0900, 47.5° latitude. Contours of F_O are shown. Oxygen is depleted by up to 40–45%.

height, and N is the buoyancy frequency. At a critical level z_c , $\bar{u} \rightarrow c$, and the wave will be absorbed there. This eddy diffusion formulation applies to $z_b < z < z_c$. Above the breaking level the wave also transfers momentum to the mean flow. The height-dependent mean flow acceleration resulting from these arguments is derived by Holton [1982].

Below the breaking level, Lindzen's parameterization was modified by Holton [1982, 1983] to mimic some of the real effects anticipated when the source generates a spectrum of waves which may break at varying levels. Below z_b ,

$$K = K(z_b) \exp \left[\frac{(z - z_b)}{H} \right]. \quad (2)$$

This modification will be adopted here. (Note: a similar modification was suggested by Lindzen [1981].) Garcia and Solomon [1985] incorporated an "efficiency factor" equal to 0.12 to reduce the Lindzen eddy diffusion and momentum deposition to match constraints on mesospheric wind and temperature distributions. They suggest the efficiency factor should be thought of as a space- and time-averaged normalization to describe the transiency of the wave-breaking process (although the work of Fritts and Lu [1993] suggests the discrepancy may be an artifact of the monochromatic wave treatment). This will be considered in the results described in the next section.

Lindzen's formulation is far from ideal. It is limited by its restriction to a monochromatic source, ignoring possible wave-wave interactions. It applies linear theory to a decidedly nonlinear problem. Values of eddy diffusion and wave drag predicted by the method are often too large. We use it in the next section to explore the local-time dependence of K suggested by the PVUVVS data (Figure 8), but do not place too much weight on the absolute values of K derived. For this reason, only qualitative conclusions are drawn about the effects of gravity wave saturation processes in the Venus thermosphere, but this is appropriate given the lack of information about the nature of the thermospheric gravity waves. This work provides some preliminary understanding of the nature of these waves and their effects on the Venus thermosphere.

5.4. Wave Sources and Local Time Asymmetries in Eddy Diffusion

In Alexander [1992], the source for the saturating thermospheric waves driving the thermospheric superrotation is placed in the Venus upper cloud deck or just above, between ~ 50 and 80 km. There is abundant evidence for waves at Venus cloud levels. Schubert [1983] gives a review of early Pioneer Venus, Mariner 10, and Venera mission observations of waves in the Venus atmosphere. Albedo features observed at cloud levels in UV photographs of Venus show many structures which have been interpreted as waves with horizontal scales ranging from about 100 km to planetary scales. One series of such markings in a Mariner 10 image appears to be an extended wave train with a 200 -km wavelength propagating nearly zonally. Circumequatorial belts with wavelengths of 500 km have been observed propagating southward with a phase speed of about 20 m s $^{-1}$. The dark horizontal Y feature has been linked to planetary-scale waves, with dark regions associated with upwelling, bright with downwelling [Del Genio and Rossow, 1990]. Albedo

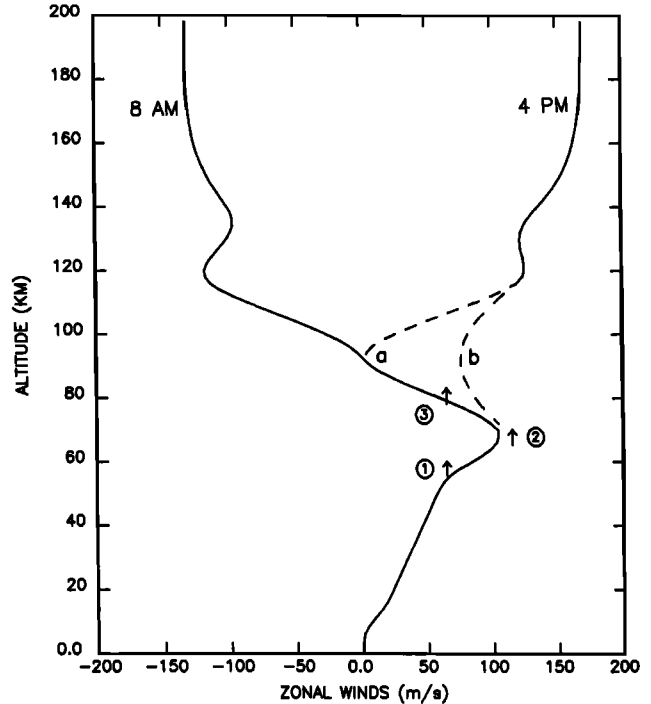


Fig. 16. Zonal wind profile from the surface of the exobase. Positive values represent westward winds. In the thermosphere, wind direction and speed depend on local time. Alternative middle atmosphere wind profiles are labeled *a* and *b* as described in the text. Arrows labeled 1, 2, and 3 denote the altitudes and phase speeds of hypothetical wave sources [after Alexander, 1992].

features interpreted as convective cells [Schubert, 1983] with horizontal scales of hundreds of kilometers have also been observed in UV images. The Vega balloons in 1985 [Linkin et al., 1986] probed the unstable layer at about 50 – 55 km altitude, and found vertical velocities of ~ 1 m s $^{-1}$ associated with convective motions there.

Schubert and Walterscheid [1984] studied propagation of gravity waves with horizontal wavelengths ~ 100 – 1000 km in the lower and middle Venus atmosphere. They found that very little wave energy forced in the lower atmosphere will propagate to the upper clouds. Westward propagating waves tend to be absorbed at critical levels. Eastward propagating waves become Doppler shifted to higher phase speeds as they propagate vertically, and become trapped in regions of low to moderate static stability. Most north-south propagating waves are also strongly attenuated in the regions of very low static stability in the lower atmosphere. The convectively unstable layer between 50 and 55 km is one likely source region for gravity waves at higher levels. Regions of strong shear in the zonal winds at cloud levels and just above provide another. Both of these would tend to generate gravity waves with large westward horizontal phase speeds, similar to the zonal wind speed at the level at which they are forced. Such an asymmetry in the spectrum of phase speeds of waves propagating into the upper atmosphere can create a local time asymmetry in eddy diffusion when these waves interact with the thermospheric winds.

The same wave source scenarios described in Alexander [1992] are applied here to study the local time variations in eddy diffusion which result. Figure 16 shows profiles of zonal wind speeds from the surface to the exobase for both

morning and afternoon local times. The lower atmosphere wind profile is taken from *Schubert and Watershed* [1984]. The thermospheric profiles are taken from *Bougher et al.* [1990], and the divergence of the profiles at these altitudes illustrates the dominant SS-AS flow pattern there. Middle atmosphere winds between the cloud tops and 90 km are widely believed to fall to near-zero velocity (profile *a*) based on observations of latitudinal temperature gradients measured by the Pioneer Venus Orbiter Infrared Radiometer and on recent ground-based measurements of winds at ~ 110 km [Goldstein et al., 1991]. An alternative profile in the middle atmosphere (profile *b*) is also shown, representing the interpretation of nighttime wind observations at ~ 99 -km altitude by *Shah et al.* [1991]. (Note that no specific alternate profile for daytime winds is shown, but the daytime profile must cross the zero point at some level below the lower thermosphere.) What follows is a discussion of three scenarios for gravity wave sources for the upper atmosphere, and corresponding local time variations in eddy diffusion predicted from the Lindzen parameterization.

The three scenarios discussed by *Alexander* [1992] are illustrated in Figure 16, where arrows mark the altitude of the wave sources in cases 1, 2, and 3, and the hypothetical wave will be assigned a phase speed equal to the zonal wind at that level. The waves are presumed to propagate into the thermosphere unless they first encounter a critical level, and thermospheric eddy diffusion coefficients are computed via the Lindzen parameterization (equations (1) and (2)), assuming a horizontal wavelength of 500 km. (The choice of 500 km is arbitrary but is similar in scale to observed waves, and similar in scale to waves used to model important vertical wave transport processes in the Earth's atmosphere by *Holton* [1982] and *Garcia and Solomon* [1985].) These assumptions follow *Alexander* [1992], so the eddy diffusion coefficients derived here will be consistent with the wave drag derived in the former.

Table 4 gives eddy diffusion coefficients at the 3-nbar pressure level derived from the application of each wave source case. No "efficiency factor" has yet been applied. Case 1 waves alone do not reproduce the correct sense of local time dependence in eddy diffusion inferred from the PVOUVS data because of critical level absorption at morning local times. However, if waves typically have phase speeds larger than the 70-km zonal wind peak (case 2) or if they are forced at levels above this peak (case 3), eddy diffusion coefficients will be much larger at morning local times than at afternoon, in accord with the PVOUVS results. The eddy diffusion coefficients calculated with the Lindzen parameterization for these three cases are huge by standards set in previous modeling efforts [Bougher et al., 1990; von Zahn et al., 1980]. In Figure 17, designed to demonstrate the local time variation in more detail, an efficiency factor of 0.1

TABLE 4. Eddy Diffusion at 3 nbar

Source	Wind Profile <i>a</i>		Wind Profile <i>b</i>	
	0800	1600	0800	1600
Case 1	0	0	0	1.1×10^7
Case 2	1.3×10^9	0	1.3×10^9	0
Case 3	5.3×10^8	0	—	—

Eddy diffusion coefficients in units of $\text{cm}^2 \text{s}^{-1}$.

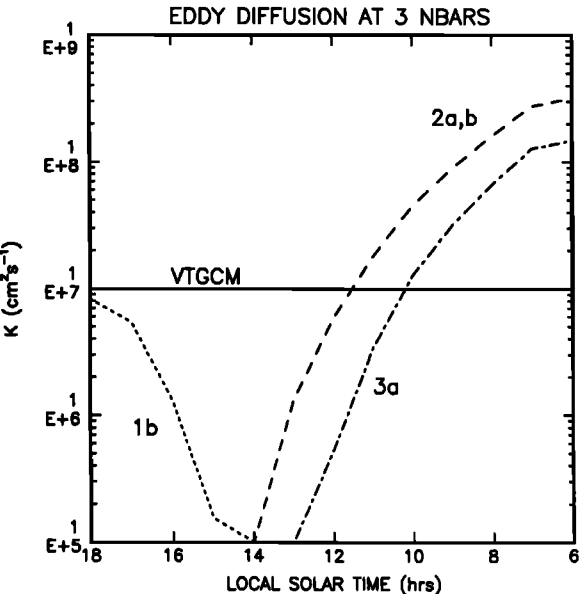


Fig. 17. Eddy diffusion (at the 3-nbar pressure level) as a function of local time for the VTGCM (solid line), and the wave sources (1, 2, and 3) and middle atmosphere wind profiles (*a* and *b*) described in the text.

is used to normalize the eddy diffusion coefficients to more reasonable values for the purpose of comparison to the VTGCM.

Figure 17 shows how eddy diffusion would vary as a function of local time for each of the three cases above. Wind and temperature profiles from the VTGCM were used to compute eddy diffusion at each hour of local solar time between 0600 and 1800 at 62.5° latitude. K at the 3-nbar pressure level is shown as a function of local time in Figure 17 for cases 1*b*, 2*a*, 2*b*, and 3*a*. (All other cases resulted in zero values.) The VTGCM eddy diffusion coefficient is also plotted for reference. It appears as a flat line because the VTGCM has no local time dependence in its eddy diffusion parameterization. In these simulations, it has been assumed that the breaking level is somewhat below the 3-nbar pressure level (~ 132 km). The 0.1 efficiency factor has been employed, as noted above. Based on the eddy diffusion sensitivity tests described in section 5.2, either of cases 2 or 3 are good candidates for reproducing the local time asymmetry observed in the PVOUVS 130-nm emission. The sum of all three cases 1 + 2 + 3 should also produce the right local time trend because the afternoon values of K in case 1 are still quite small.

The eddy diffusion coefficients in Figure 17 are consistent with the wave drag, in Figure 2 of *Alexander* [1992], which was derived to explain the thermospheric superrotation. These two complementary results provide strong support for the cloud-level wave source hypothesis for saturating thermospheric waves.

The cloud-level wave saturation mechanism does not explain the latitudinal structure observed in the PVOUVS results (Figure 8). However, the observed structure in O can be reconciled with the observations of the thermospheric superrotation within the context of this hypothesis, and this will be discussed further in section 6.4.

6. SUMMARY AND DISCUSSION

6.1. Summary of Model Development

The analysis of the 130-nm images relies on the model developed in section 3. The essential components of this model are (1) the neutral model thermosphere, (2) the photoelectron excitation model, (3) the solar 130-nm flux estimation, (4) the radiative transfer model, and (5) the solar activity correlations. Each of these is briefly summarized below.

The neutral thermosphere is a synthesis of the empirical VTS3 and the VTGCM. The VTS3 vertical profile was chosen because it better reflects the magnitude of the oxygen density in the important regions of the thermosphere. The VTGCM was used as a guide to describe the dayside distribution of O because the VTS3 is only based on measurements at latitudes below 20°. The spherical harmonic fit at higher latitudes in the VTS3 creates patterns in the oxygen distribution which are not observed and would confuse interpretation in a data/model comparison. The VTGCM computes the density distributions nearly self-consistently with all of the important dynamic, thermodynamic, and chemical processes, however the magnitude of f_O in the VTGCM result is about 40% lower than the accepted values (VTS3 and VIRA).

The photoelectron excitation model is state of the art, including the effects of electron transport with a two-stream approximation. It computes cascade from important higher lying states in the oxygen atom explicitly, not relying on ad hoc cascade enhancement factors over the optically thin cross sections. The model relies heavily on terrestrial experience with these processes [Solomon et al., 1988; Solomon and Abreu, 1989], where it has been well tested against airglow observations.

The estimation of the solar 130-nm flux is based primarily on the 1982 and 1983 rocket measurements of Mount and Rottman [1985]. The solar line profiles are taken from Bruner et al. [1970], which are perhaps now considered out of date [Gladstone, 1988; R. R. Meier, personal communication, 1992]. However, considerable uncertainties in the line shape still exist and the effect of updating the profile shape on our model result should be much less than the uncertainty in the PVOUVS intensities.

The radiative transfer model is R. R. Meier's [Meier and Lee, 1982; Meier, 1991]. It has been modified from the original plane-parallel version to account for spherical effects. These are only important at viewing angles larger than ~75°. The model employs a Monte Carlo technique and includes partial frequency redistribution and angle dependency in the scattering process. It also includes the effect of thermospheric temperature gradients on the optical depths. The model has previously been tested against airglow observations of the thermospheres of Earth [Meier et al., 1985; Morrison and Meier, 1988], Venus [Meier et al., 1983; Paxton and Meier, 1986], and Mars [Stewart et al., 1992].

Solar activity variations have been incorporated into the model empirically using a correlation between the observed 130-nm brightness and the index $VF_{10.7}$ [Brace et al., 1988] derived from measurements of the Langmuir probe instruments on the Pioneer Venus orbiter. This is an effective technique for the examination of the anomalous features in O and B_{130} but circumvents the separate but interesting ques-

tion of how the global atomic oxygen densities vary with solar activity.

These model components are assembled for comparison to the data. The result is a model which accurately describes the global-scale trends in the 130-nm images. The differences are, however, important and can be interpreted in terms of the large-scale structure and dynamics of the thermosphere.

6.2. Summary of Results and Interpretation

The solar-locked features identified in the data/model comparison appear as a local time asymmetry in B_{130} and O at latitudes poleward of 30° (Figure 8). Oxygen densities at the evening terminator are typically a factor of 2 higher than those at the morning terminator. The pattern is remarkably persistent, appearing in every image examined spanning a 10-year period (Figure 9). This asymmetry in O has never before been observed or predicted in the global thermospheric models (although an asymmetry in O^+ has been observed at 200 km [Taylor et al., 1980]). The in situ measurements did not cover extratropical latitudes, and the general circulation models (which include superrotating winds) do not predict it. This persistent pattern must be a signature of some very fundamental unknown process occurring in the Venus thermosphere.

A hypothesis for explaining this local time asymmetry in the thermospheric oxygen densities is developed in section 5. If gravity waves originating in the lower atmosphere at cloud level are propagating into the thermosphere and saturating there, they can generate a pattern of turbulence asymmetric in local time. Turbulence is frequently parameterized in atmospheric models with eddy diffusion. This process will tend to mix atomic oxygen down the O mixing ratio gradient which is downward in altitude, and can result in depletion of O over a wide range of altitudes in the thermosphere. This mechanism for varying O densities locally in patterns of latitude and local time has been tested in the VTGCM, although the benchmark VTGCM calculation [Bougher et al., 1988, 1990] employs a constant dayside distribution of eddy diffusion.

The key to developing the observed local time trend lies in postulating a fairly steady supply of cloud-level waves propagating into the thermosphere. These waves will preferentially be forced with westward phase speeds similar to the zonal wind speeds in the clouds. The Lindzen [1981] parameterization for eddy diffusion is used to examine the resulting local time asymmetries. The magnitude of the eddy diffusion in this model varies strongly with the difference between the thermospheric mean wind speed and the phase speed of the wave (equation (1)), so that the eddy diffusion coefficients at morning local times should be much larger than at corresponding afternoon times. The VTGCM tests suggest the derived eddy diffusion asymmetry should be sufficient to generate the observed oxygen variations (Figure 17). This basic result is a consequence of the interaction of westward propagating waves with the predominantly SS-AS circulation pattern in the thermosphere.

The waves postulated to explain the local time asymmetry in eddy diffusion will also deposit momentum in the thermosphere. This work, in conjunction with Alexander [1992], shows that the same mechanism producing the local time asymmetries observed in the 130-nm images may also explain the superrotation component of the thermospheric

winds. This exciting result lends strength to the original hypothesis, since it can explain both the oxygen and wind asymmetries at once.

6.3. Earth Analogies

Transport of energy and momentum between atmospheric regions with gravity waves as the vehicle is a well established process in the Earth's atmosphere. Reviews by Fritts [1984, 1989] describe the observations and development of the theory which have led to an understanding of the importance of gravity wave saturation processes in the Earth's middle atmosphere.

The linear saturation theory developed by Lindzen [1981] has been used by Holton [1982, 1983] to demonstrate a first-order effect on the general circulation of the mesosphere. Garcia and Solomon [1985] coupled these gravity wave saturation effects to the chemical composition in the mesosphere and found solutions consistent with both dynamical and airglow observations. They note the sensitivity of oxygen species in the mesosphere to both large- and small-scale transport processes, and use this fact to further constrain the gravity wave effects in the mesosphere and lower thermosphere. The ideas of Lindzen were extended by Dunkerton [1982] to explain the mesopause semiannual oscillation. The idea of momentum deposition by waves with seasonally varying phase speeds is fundamental to the understanding of this oscillation in the winds at the mesopause. A similar mechanism was previously employed to explain the quasi-biennial oscillation of the equatorial stratosphere [Holton and Lindzen, 1972]. Studies such as these have shown gravity wave saturation effects to be of great importance in understanding the dynamics and composition of the middle atmosphere and lower thermosphere of the Earth.

6.4. Outstanding Questions

The latitudinal variations in the brightness patterns evident in Figure 8 are not explained by the cloud-level source hypothesis put forth in this paper. The local time asymmetry in atomic oxygen density essentially disappears at equatorial latitudes less than 30°. The explanation for this could be latitudinal variations in the source region such as a preference for excitation at the latitude of the cloud-level jet at 50–60°. Alternatively, latitudinal variations might be related to differences in the degree of filtering of the waves in the middle atmosphere or lower thermosphere. A third possibility suggested by R. W. Zurek (personal communication, 1991) is that the propagating tides might selectively influence the stability of smaller-scale waves in the thermosphere. The Venus tides are, however, not well understood, especially at thermospheric altitudes [Pechmann and Ingersoll, 1984], and the preference for a high-latitude effect would not be expected. Another possible explanation is a variation of breaking level with latitude. If the waves break higher at low latitudes (say, at 150 km), they would have much less impact on oxygen densities, but could still force the thermospheric superrotation. In any case, the thermospheric superrotation is best constrained only above 150 km via diurnal density patterns in H and He. No constraints on details such as the latitudinal variation in the superrotation speeds exist, so the latitudinal variations observed in the PVOUVS and the superrotation observations are not a priori unresolvable

within the context of the gravity wave saturation mechanism proposed here.

Questions pertaining to the magnitude of the energy and momentum transported from Venus' lower to upper atmosphere remain unanswered. Given the lack of information about the sources and characteristics of vertically propagating gravity waves in the thermosphere, these cannot be answered directly at this time. Thermospheric evidence of the effects of the saturation processes can, however, be used to constrain models of the mean flow effects, and the result could further the understanding of the wave properties. The VTGCM is well suited to handling this problem, given a physically meaningful parameterization for eddy diffusion and wave drag. The results of the work presented here using Lindzen's [1981] parameterization coupled to the results in Alexander [1992], could offer an improvement over the current VTGCM parameterization by providing a physical mechanism for the superrotation and a means for a self-consistent coupling of the wave drag and eddy diffusion parameterizations. Currently, a spectral parameterization for gravity wave momentum and energy fluxes is being developed by Fritts and others [Fritts and VanZandt, 1993; Fritts and Lu, 1993], which promises to be a great advance over the earlier monochromatic parameterizations. The gravity wave spectrum they employ is modeled after Earth observational evidence, but a similar parameterization might be developed for application to the Venus upper atmosphere.

Acknowledgments. This work was supported by NASA grant NAG2-504. The authors would like to thank Anthony Del Genio and another reviewer for their careful reviews and thought-provoking comments.

REFERENCES

- Alexander, M. J., A mechanism for the Venus thermospheric superrotation, *Geophys. Res. Lett.*, 19, 2207, 1992.
- Bouger, S. W., R. E. Dickinson, E. C. Ridley, R. G. Roble, A. F. Nagy, and T. E. Cravens, Venus mesosphere and thermosphere, II, Global circulation, temperature, and density variations, *Icarus*, 68, 284, 1986.
- Bouger, S. W., R. E. Dickinson, E. C. Ridley, and R. G. Roble, Venus mesosphere and thermosphere, III, Three-dimensional general circulation with coupled dynamics and composition, *Icarus*, 73, 545, 1988.
- Bouger, S. W., J. C. Gérard, A. I. F. Stewart, and C. G. Fesen, The Venus nitric oxide night airglow: Model calculations based on the Venus thermospheric general circulation model, *J. Geophys. Res.*, 95, 6271, 1990.
- Brace, L. H., W. R. Hoegy, and R. F. Theis, Solar EUV measurements at Venus based on photoelectron emission from the Pioneer Venus Langmuir probe, *J. Geophys. Res.*, 93, 7282, 1988.
- Brinton, H. C., H. A. Taylor, Jr., H. B. Neumann, H. G. Mayr, A. F. Nagy, T. E. Cravens, and D. F. Strobel, Venus nighttime hydrogen bulge, *Geophys. Res. Lett.*, 7, 865, 1980.
- Brune, W. H., G. H. Mount, and P. D. Feldman, Vacuum ultraviolet spectrophotometry and effective temperatures of hot stars, *Astrophys. J.*, 227, 884, 1979.
- Bruner, E. C., Jr., R. A. Jones, W. A. Rense, and G. E. Thomas, Ultraviolet line profiles of O I in the solar spectrum, *Astrophys. J.*, 162, 281, 1970.
- Del Genio, A. D., and W. B. Rossow, Planetary-scale waves and the cyclic nature of cloud top dynamics on Venus, *J. Atmos. Sci.*, 47, 293, 1990.
- Dickinson, R. E., Circulation and thermal structure of the Venusian thermosphere, *J. Atmos. Sci.*, 28, 885, 1971.
- Dickinson, R. E., and E. C. Ridley, A numerical model for the

- dynamics and composition of the Venusian thermosphere, *J. Atmos. Sci.*, **32**, 1219, 1975.
- Dickinson, R. E., and E. C. Ridley, Venus mesosphere and thermosphere temperature structure, II, Day-night variations, *Icarus*, **30**, 163, 1977.
- Doering, J. P., and S. O. Vaughan, Absolute experimental differential and integral cross sections for atomic oxygen, I, The ($^3P - ^3S^0$) transition (1304 Å) at 100 eV, *J. Geophys. Res.*, **91**, 3279, 1986.
- Dunkerton, T. J., Theory of the mesopause semiannual oscillation, *J. Atmos. Sci.*, **39**, 2681, 1982.
- Fox, J. L., and S. W. Bougher, Structure, luminosity and dynamics of the Venus thermosphere, *Space Sci. Rev.*, **55**, 357, 1991.
- Fritts, D. C., Gravity wave saturation in the middle atmosphere: A review of theory and observations, *Rev. Geophys.*, **22**, 275, 1984.
- Fritts, D. C., A review of gravity wave saturation processes, effects and variability in the middle atmosphere, *Pure Appl. Geophys.*, **130**, 343, 1989.
- Fritts, D. C., and W. Lu, Spectral estimates of gravity wave energy and momentum fluxes, II, Parameterization of wave forcing and variability, *J. Atmos. Sci.*, in press, 1993.
- Fritts, D. C., and T. E. VanZandt, Spectral estimates of gravity wave energy and momentum fluxes, I, Energy dissipation, acceleration, and constraints, *J. Atmos. Sci.*, in press, 1993.
- Garcia, R. R., and S. Solomon, The effect of breaking gravity waves on the dynamics and chemical composition of the mesosphere and lower thermosphere, *J. Geophys. Res.*, **90**, 3850, 1985.
- Gladstone, G. R., UV resonance line dayglow emissions on Earth and Jupiter, *J. Geophys. Res.*, **93**, 14,623, 1988.
- Goldstein, J. J., M. J. Mumma, T. Kostiuk, D. Deming, F. Espenak, and D. Zipoy, Absolute wind velocities in the lower thermosphere of Venus using infrared heterodyne spectroscopy, *Icarus*, **94**, 45, 1991.
- Gulcicek, E. E., and J. P. Doering, Absolute differential and integral electron excitation cross sections for atomic oxygen, 5, Revised values for the $^3P \rightarrow ^3S^0$ (1304 Å) and $^3P \rightarrow ^3D^0$ (989 Å) transitions below 30 eV, *J. Geophys. Res.*, **93**, 5879, 1988.
- Gulcicek, E. E., J. P. Doering, and S. O. Vaughan, Absolute differential and integral electron excitation cross sections for atomic oxygen, 6, The $^3P \rightarrow ^3P$ and $^3P \rightarrow ^5P$ transitions from 13.87 to 100 eV, *J. Geophys. Res.*, **93**, 5885, 1988.
- Hedin, A. E., H. B. Niemann, W. T. Kasprzak, and A. Seiff, Global empirical model of the Venus thermosphere, *J. Geophys. Res.*, **88**, 73, 1983.
- Hinteregger, H. E., K. Fukui, and B. R. Gibson, Observational, reference, and model data on solar EUV, from measurements on AE-E, *Geophys. Res. Lett.*, **8**, 1147, 1981.
- Holton, J. R., The role of gravity wave induced drag and diffusion in the momentum budget of the mesosphere, *J. Atmos. Sci.*, **39**, 791, 1982.
- Holton, J. R., The influence of gravity wave breaking on the general circulation of the middle atmosphere, *J. Atmos. Sci.*, **40**, 2497, 1983.
- Holton, J. R., and R. S. Lindzen, An updated theory for the quasi-biennial cycle of the tropical stratosphere, *J. Atmos. Sci.*, **29**, 1076, 1972.
- Jackman, C. H., R. H. Garvey, and A. E. S. Green, Electron impact on atmospheric gases, I, Updated cross sections, *J. Geophys. Res.*, **82**, 5081, 1977.
- Keating, G. M., J. Y. Nicholson III, and L. R. Lake, Venus upper atmosphere structure, *J. Geophys. Res.*, **85**, 7941, 1980.
- Keating, G. M., et al., Models of Venus neutral upper atmosphere: Structure and composition, *Adv. Space Res.*, **5**(11), 117, 1985.
- Lawrence, G. M., Photodissociation of CO₂ to produce CO ($a^3 II$), *J. Chem. Phys.*, **56**, 3435, 1972.
- Lee, J.-S., and R. R. Meier, Angle-dependent frequency redistribution in a plane-parallel medium: External source case, *Astrophys. J.*, **240**, 185, 1980.
- Lindzen, R. S., Turbulence and stress owing to gravity wave and tidal breakdown, *J. Geophys. Res.*, **86**, 9707, 1981.
- Linkin, V. M., et al., VEGA balloon dynamics and vertical winds in the Venus middle cloud region, *Science*, **231**, 1417, 1986.
- Massie, S. T., D. M. Hunten, and D. R. Sowell, Day and night models of the Venus thermosphere, *J. Geophys. Res.*, **88**, 3955, 1983.
- Mayr, H. G., I. Harris, R. E. Hartle, and W. R. Hoegy, Diffusion model for the upper atmosphere of Venus, *J. Geophys. Res.*, **83**, 4411, 1978.
- Mayr, H. G., I. Harris, H. B. Niemann, H. C. Brinton, N. W. Spencer, H. A. Taylor, Jr., R. E. Hartle, W. R. Hoegy, and D. M. Hunten, Dynamic properties of the thermosphere inferred from Pioneer Venus mass spectrometer measurements, *J. Geophys. Res.*, **85**, 7841, 1980.
- Mayr, H. G., I. Harris, D. R. Stevens-Rayburn, H. B. Niemann, H. A. Taylor, Jr., and R. E. Hartle, On the diurnal variations in the temperature and composition: A three-dimensional model with superrotation, *Adv. Space Res.*, **5**(9), 109, 1985.
- Meier, R. R., Ultraviolet spectroscopy and remote sensing of the upper atmosphere, *Space Sci. Rev.*, **58**, 1, 1991.
- Meier, R. R., and J.-S. Lee, An analysis of the O I 1304 Å dayglow using a Monte Carlo resonant scattering model with partial frequency redistribution, *Planet. Space Sci.*, **30**, 439, 1982.
- Meier, R. R., D. E. Anderson, Jr., and A. I. F. Stewart, Atomic oxygen emissions observed from Pioneer Venus, *Geophys. Res. Lett.*, **10**, 214, 1983.
- Meier, R. R., R. R. Conway, D. E. Anderson, Jr., P. D. Feldman, R. W. Eastes, E. P. Gentieu, and A. B. Christensen, The ultraviolet dayglow at solar maximum, 3, Photoelectron-excited emissions of N₂ and O, *J. Geophys. Res.*, **90**, 6608, 1985.
- Mengel, J. G., D. R. Stevens-Rayburn, H. G. Mayr, and I. Harris, Non-linear three dimensional spectral model of the Venusian thermosphere with super-rotation, II, Temperature, composition and winds, *Planet. Space Sci.*, **37**, 707, 1989.
- Morrison, M. D., and R. R. Meier, The O I 989 and 1173 Å multiplets in the dayglow, *Planet. Space Sci.*, **36**, 987, 1988.
- Mount, G. H., and G. J. Rottman, The solar spectral irradiance 1200–3184 Å near solar maximum: July 15, 1980, *J. Geophys. Res.*, **86**, 9193, 1981.
- Mount, G. H., and G. J. Rottman, Solar absolute spectral irradiance 118–300 nm: July 25, 1983, *J. Geophys. Res.*, **90**, 13,031, 1985.
- Nagy, A. F., and P. M. Banks, Photoelectron fluxes in the ionosphere, *J. Geophys. Res.*, **75**, 6260, 1970.
- Niemann, H. B., W. T. Kasprzak, A. E. Hedin, D. M. Hunten, and N. W. Spencer, Mass spectrometric measurements of the neutral gas composition of the thermosphere and exosphere of Venus, *J. Geophys. Res.*, **85**, 7817, 1980.
- Paxton, L. J., and R. R. Meier, Reanalysis of Pioneer orbiter ultraviolet spectrometer data: O I 1304 intensities and atomic oxygen densities, *Geophys. Res. Lett.*, **13**, 229, 1986.
- Pechmann, J. B., and A. P. Ingersoll, Thermal tides in the atmosphere of Venus: Comparison of model results with observations, *J. Atmos. Sci.*, **41**, 3290, 1984.
- Samson, J. A. R., and P. N. Pareek, Absolute photoionization cross sections of atomic oxygen, *Phys. Rev. A.*, **31**, 1470, 1985.
- Sawada, T., D. J. Strickland, and A. E. S. Green, Electron energy deposition in CO₂, *J. Geophys. Res.*, **77**, 4812, 1972a.
- Sawada, T., D. L. Sellin, and A. E. S. Green, Electron impact excitation cross sections and energy degradation in CO, *J. Geophys. Res.*, **77**, 4819, 1972b.
- Schubert, G., General circulation and the dynamical state of the Venus atmosphere, in *Venus*, edited by D. M. Hunten, et al., 681 pp., University of Arizona Press, Tucson, 1983.
- Schubert, G., and R. L. Walterscheid, Propagation of small-scale acoustic-gravity waves in the Venus atmosphere, *J. Atmos. Sci.*, **41**, 1202, 1984.
- Shah, K. P., D. O. Muhleman, and G. L. Berge, Measurement of winds in Venus' upper mesosphere based on Doppler shifts of the 2.6-mm ¹²CO line, *Icarus*, **93**, 96, 1991.
- Solomon, S. C., and V. J. Abreu, The 630 nm dayglow, *J. Geophys. Res.*, **94**, 6817, 1989.
- Solomon, S. C., P. B. Hays, and V. J. Abreu, The auroral 6300 Å emission: Observations and modeling, *J. Geophys. Res.*, **93**, 9867, 1988.
- Stewart, A. I. F., Design and operation of the Pioneer Venus orbiter ultraviolet spectrometer, *IEEE Trans. Geosci. Remote Sensing, GE-18*, 65, 1980.
- Stewart, A. I., D. E. Anderson, Jr., L. W. Esposito, and C. A. Barth, Ultraviolet spectroscopy of Venus: Initial results from the Pioneer Venus orbiter, *Science*, **203**, 777, 1979.
- Stewart, A. I. F., J.-C. Gérard, D. W. Rusch, and S. W. Bougher, Morphology of the Venus ultraviolet night airglow, *J. Geophys. Res.*, **85**, 7861, 1980.

- Stewart, A. I. F., M. J. Alexander, R. R. Meier, L. J. Paxton, S. W. Bouger, and C. G. Fesen, Atomic oxygen in the Martian thermosphere, *J. Geophys. Res.*, **97**, 91, 1992.
- Strickland, D. J., The transport of resonance radiation in a nonisothermal medium—The effect of a varying Doppler width, *J. Geophys. Res.*, **84**, 5890, 1979.
- Swartz, W. E., Optimization of energetic electron energy degradation calculations, *J. Geophys. Res.*, **90**, 6587, 1985.
- Taylor, H. A., Jr., H. C. Brinton, S. J. Bauer, R. E. Hartle, P. A. Cloutier, and R. E. Daniell, Jr., Global observations of the composition and dynamics of the ionosphere of Venus: Implications for the solar wind interaction, *J. Geophys. Res.*, **85**, 7765, 1980.
- Torr, M. R., and D. G. Torr, Ionization frequencies for solar cycle 21: Revised, *J. Geophys. Res.*, **90**, 6675, 1985.
- Torr, M. R., D. G. Torr, R. A. Ong, and H. E. Hinteregger, Ionization frequencies for major thermospheric constituents as a function of solar cycle 21, *Geophys. Res. Lett.*, **6**, 771, 1979.
- Vaughan, S. O., and J. P. Doering, Absolute experimental differential and integral electron excitation cross sections for atomic oxygen, 2, The ($^3P \rightarrow ^3S^0$) transition (1304 Å) from 16.5 to 200 eV with comparison to atomic hydrogen, *J. Geophys. Res.*, **91**, 13,755, 1986.
- Vaughan, S. O., and J. P. Doering, Absolute experimental differential and integral electron excitation cross sections for atomic oxygen, 3, The ($^3P \rightarrow ^3D^0$) transition (989 Å) from 20 to 200 eV with improved values for the ($^3P \rightarrow ^3S^0$) transition (1304 Å), *J. Geophys. Res.*, **92**, 7749, 1987.
- Vaughan, S. O., and J. P. Doering, Absolute experimental differential and integral electron excitation cross sections for atomic oxygen, 4, The ($^3P \rightarrow 3s'' ^3P^0$), ($^3P \rightarrow 2s2p^5 ^3P^0$), ($^3P \rightarrow 4d' ^3P^0$) autoionizing transitions (878, 792, and 770 Å) and five members of the ($^3P \rightarrow nd ^3D^0$) Rydberg series (1027 Å), *J. Geophys. Res.*, **93**, 289, 1988.
- von Zahn, U., K. H. Fricke, D. M. Hunten, D. Krankowsky, K. Mauersberger, and A. O. Nier, The upper atmosphere of Venus during morning conditions, *J. Geophys. Res.*, **85**, 7829, 1980.
- Zipf, E. C., and P. W. Erdman, Electron impact excitation of atomic oxygen: Revised cross sections, *J. Geophys. Res.*, **90**, 11,087, 1985.
-
- M. J. Alexander, Department of Atmospheric Sciences, AK-40, Seattle, WA 98195.
- S. W. Bouger, Lunar and Planetary Laboratory, University of Arizona, Tucson, AZ 85721.
- S. C. Solomon and A. I. F. Stewart, Laboratory for Atmospheric and Space Physics, University of Colorado, Boulder, CO 80309-0392.

(Received August 20, 1992;
revised February 21, 1993;
accepted March 4, 1993.)